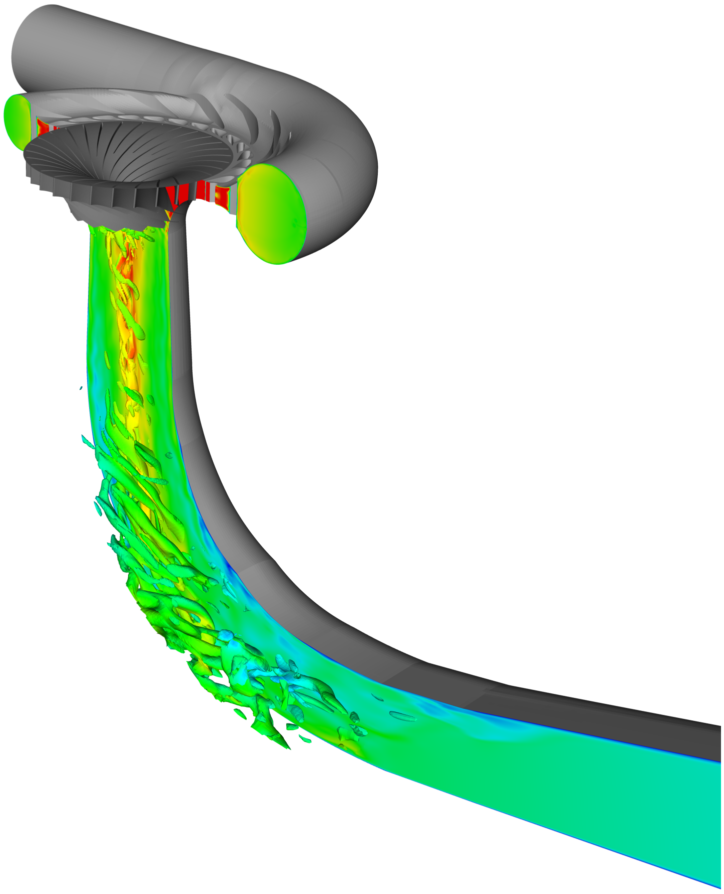

Simulations of the flow-driven rotation of the Francis-99 turbine runner

Evaluating the use of PANS and ILES turbulence modelling

Master's thesis in Applied Mechanics

ERIK KRANE

Department of Applied Mechanics
CHALMERS UNIVERSITY OF TECHNOLOGY
Göteborg, Sweden 2015

MASTER'S THESIS IN APPLIED MECHANICS

Simulations of the flow-driven rotation of the Francis-99 turbine runner

Evaluating the use of PANS and ILES turbulence modelling

ERIK KRANE

Department of Applied Mechanics
Division of Fluid Dynamics
CHALMERS UNIVERSITY OF TECHNOLOGY

Göteborg, Sweden 2015

Simulations of the flow-driven rotation of the Francis-99 turbine runner
Evaluating the use of PANS and ILES turbulence modelling
ERIK KRANE

Master's thesis 2015:56
ISSN 1652-8557
Department of Applied Mechanics
Division of Fluid Dynamics
Chalmers University of Technology
SE-412 96 Göteborg
Sweden
Telephone: +46 (0)31-772 1000

Cover:
Isosurfaces of Q-criterion of 200 and a y=0 plane, both coloured by velocity magnitude.

Chalmers Reproservice
Göteborg, Sweden 2015

Simulations of the flow-driven rotation of the Francis-99 turbine runner
Evaluating the use of PANS and ILES turbulence modelling
Master's thesis in Applied Mechanics
ERIK KRANE
Department of Applied Mechanics
Division of Fluid Dynamics
Chalmers University of Technology

Abstract

Today, the steadily increasing amount of renewable energy production is changing the way hydraulic power plants are used. The intermittent generation of wind and solar power creates instabilities in the electric grid that need to be countered in a fast and reliable way. Hydro power plants are good at changing power output by simply adjusting the flow through the turbine. They are, however, not designed for that amount of transient loads, which will result in a lower efficiency at off-design operating conditions and a higher degree of fatigue.

In this thesis, the flow in a high-head Francis turbine is investigated. The turbine is a model of a full scale prototype turbine operating in Norway. It is in the spirit of the Francis-99 workshop series, aimed to determine the state of the art in high-head Francis turbine simulations, that this thesis is written. The geometry and experimental results of the Francis-99 turbine that are used in this work are freely available at the Luleå University of Technology homepage. The focus of the thesis is two-fold; firstly, the accuracy of a number of turbulence modelling methods are investigated at the best efficiency operating condition. The turbulence modelling approaches used are the k-ε RNG and k-ω SST URANS models, together with the k-ω SST PANS and ILES methods. Secondly, the implementation of flow driven runner rotation for the purpose of transient operation simulations is evaluated. The operating condition used to test the functionality of this implementation is a load-rejection case. All simulations are performed in an unsteady framework using the finite volume code FOAM-extend 3.1, which is a highly modifiable, open-source CFD code. The geometry comprises all parts from the spiral casing to the draft tube outlet, with the full runner and all guide vanes included.

All turbulence models perform similarly when comparing the velocity profiles, with the ILES and k-ω SST models correlating best with the experiments. The strong swirl appearing in most of the simulations presented at the 2014 workshop does not appear in the present work, which is closer to the experimental results. The turbine head is over-predicted by 10-20% and the extracted shaft work by 12-21%, resulting in good agreement with experimental efficiency. The main frequencies of the pressure probes agree with experiments, and correspond to the blade passing frequencies of the runner blades and guide vanes. The implementation of the flow-driven rotation show robustness and promising trends, but further investigation is needed before comments can be made on accuracy.

Keywords: Francis-99, CFD, Hydropower, Francis turbine, FOAM-extend, PANS, ILES, Turbulence modelling, Flow-driven, Mesh motion

Acknowledgements

I would like to express my gratitude to Håkan Nilsson for being the examiner and supervisor during this thesis and for much support and many fruitful discussions. I would also like to thank Ardalan Javadi for the great advice in simulating turbomachinery and the usage of FOAM-extend; and Lucien Stoessel for providing very useful tools and tips concerning the Francis-99 turbine. Many thanks also go to the Swedish national infrastructure of computing (SNIC), Chalmers centre for science and engineering (C^3SE) and the National supercomputer centre (NSC) at Linköping University for providing the computational resources making this thesis at all possible. The relaxed and friendly atmosphere at the fluid dynamics division at Chalmers have been a great help during this period and many interesting topics have been discussed in the coffee room.

Finally, I would like to thank my friends and family for the support and advice they have contributed with throughout these months.

Nomenclature

Variable	Symbol	Unit
ρ	Density	kg/m^3
ν	Kinematic viscosity	m^2/s
p	Pressure	Pa
N	Rotational speed	rpm
D	Diameter	m
θ	Angular position	rad
ω	Angular speed	rad/s
α	Angular acceleration	rad/s^2
f	Frequency	1/s
T	Torque	Nm
η_h	Hydraulic efficiency	-
c_θ	Tangential velocity	m/s
y^+	Dimensionless wall distance	-
ν_t	Eddy viscosity	m^2/s
k	Turbulence kinetic energy	m^2/s^2
ε	Turbulence dissipation rate	m^2/s^3
ω	Specific turbulence dissipation rate	1/s
Λ	Turbulence length scale	m

Abbreviation	Description
BEP	Best Efficiency Point
CFD	Computational Fluid Dynamics
RANS	Reynolds Averaged Navier-Stokes
PANS	Partially Averaged Navier-Stokes
LES	Large Eddy Simulation
ILES	Implicit Large Eddy Simulation
MILES	Monotone Integrated Large Eddy simulation
ZLES	Zonal Large Eddy Simulation
SGS	Sub-Grid Scale
VLES	Very Large Eddy Simulation
NFV	Non-oscillatory Finite-Volume
RSM	Reynolds Stress Model
EARSM	Explicit Algebraic Reynolds Stress Model
RNG	ReNormalisation Group
SST	Shear Stress Transport
GGI	General Grid Interface
PCG	Preconditioned Conjugate Gradient
PBiCG	Preconditioned Bi-Conjugate Gradient
GAMG	Geometric-Algebraic Multi-Grid
IEC	International Electrotechnical Commission
LDA	Laser Doppler Anemometry
FFT	Fast Fourier Transform

Index or Symbol	Description
u_i	Vector in tensor notation
$\bar{u}$	Time-averaged quantity
u'	Fluctuating quantity
$\|u\|$	Magnitude

Contents

1 Introduction

1.1 Background

Traditionally, hydroelectric power have been used mainly as a base power source, continuously providing the electric grid with energy. It is also the single energy production system that can be efficiently used as energy storage in the form of dams. This, combined with the ability to rapidly change the power output of any single turbine makes it ideal to use as a grid modulator. With the introduction of intermittent energy sources, such as wind and solar power, the need for grid modulation has increased. When hydroelectric power plants are used to stabilise the electric grid the turbines will no longer run at the point of best efficiency, and the operating conditions will likely need to change several times per day. Consequently, the study of transient operation and off-design performance of hydroelectric turbines is becoming increasingly important. This is the motivation for the Francis-99 workshop series, which aims to determine the state of the art in high head Francis turbine simulations. The subject of the workshops is the simulation of the *Tokke* model turbine designed at NTNU, Trondheim, Norway. The first workshop took place in December 2014 at NTNU, focusing on steady and unsteady simulations of the steady operation of the turbine. The focus for the second workshop, planned for December 2016, is the simulation of transient operation. For the third and final workshop occasion fluid-structure interaction is the main focus, planned for 2018.

1.2 Previous work

- In the work of Trivedi et al. [38] numerical and experimental analyses of the Francis-99 turbine were performed. The experimental results have created a base for the development and analysis of numerical methods applied to high-head Francis turbines. The numerical simulations show good prediction of hydraulic efficiency at BEP but deviate by $11-14\%$ at part load depending on turbulence model. A majority of the papers submitted to the 2014 workshop arrive at similar results. The performance is well predicted at the point of best efficiency and to some extent at high load. At part load, however, the efficiency is not accurately predicted by turbine simulations alone but a model or simulation of the seal friction and leakage flow is required. This is employed by Mössinger, Jester-Zürker, and Jung [25] in the form of an analytic relation included in the CFD simulations. Celic and Ondracka [5] opt for another path and include the full seal geometry. Both methods increase the accuracy of the hydraulic efficiency at part load, and in the full 3D leakage simulations the efficiency becomes lower than the experimental values. When comparing the draft tube velocity profiles the results are reversed, and most simulations predict the velocity profiles well at part load, while the deviations are large at BEP. In several papers [1, 24, 36, 26] a strong swirl was present at the center of the draft tube, which does not appear in the experiments. This high swirl is apparent to some extent in both steady and unsteady simulations. Some authors have managed to reduce the center swirl velocity by the use of scale-resolving turbulence models such as the filtered k-ω SST model of Gyllenram [14] used by Stoessel [36] and a zonal LES method used by Jost et al. [17], applying LES modelling only in the draft tube and URANS everywhere else.

The aim for more accurate simulations have driven the development of variable resolution (VR) turbulence models, where the largest turbulent scales are resolved and the small are modelled. The PANS method suggested by Girimaji [10] use a specified ratio of unresolved-to-resolved turbulence scales for filtering. In its original form the derivation of the PANS equations was based on the k-ε turbulence model, but have later been used with a number of different turbulence models. Zreik [42] showed that a k-ω based PANS model was superior to the original in the flow past two cylinders. A PANS model for wall-bounded flow, developed from the k-ε-ζ-f model [15], have also shown superiority to LES for some cases [18] with near-wall grid resolution too coarse for LES.

A method similar to LES but without sub-grid turbulence model have been suggested by Boris [4]. It is called MULES or ILES and uses limited second order numerical discretisation schemes rather than the central-differencing scheme commonly used in LES. The dissipation of the explicit sub-grid model is hence replaced by an implicit dissipation from the numerical scheme. As the only way to control the behaviour of the ILES model, the selection of discretisation schemes are obviously of great importance. A family of schemes, called Non-oscillatory Finite Volume (NFV) schemes that are known to work well for ILES are explained in great detail by Margolin, Rider, and Grinstein [22], for example MPDATA (Multidimensional Positive Definite Advection Transport Algorithm) by Smolarkiewicz [30, 31] and MUSCL (Monotonic Upstream-Centered Scheme for Conservation Laws) by van Leer [21].

The use of OpenFOAM and FOAM-extend as a tool for simulation of turbomachinery and hydro-power applications have been evaluated and validated by several authors. In 2006, Nilsson [27] found that OpenFOAM compared well to CFX and experimental results of a Kaplan turbine. More recent versions of the code have evaluated by Petit [29] among others. The development of tools for enhancing the simulations of hydro-turbines, such as an MRF solver, GGI and mixingPlane coupling interfaces and specialised boundary conditions, were presented by Page, Beaudoin, and Giroux [28].

The transient operation of hydroelectric turbines have been extensively researched using experimental methods, in the Tokke turbine by Trivedi et al. [39]. To perform CFD simulations with changing operating conditions requires special software tools and large computational resources as transients take place in a number of seconds, or tens of seconds. An implementation of flow-driven mesh rotation in the OpenFOAM framework have been developed by Chen et al. [6] for the application on wind turbine simulations. A similar implementation for FOAM-extend is presented by Krane [19], which is the implementation used in this thesis.

1.3 Purpose and aim

The aim is to further develop the numerical methods of predicting the flow behaviour and performance of hydroelectric turbines, specifically the high head Francis-99 turbine. Unsteady simulations using URANS turbulence modelling at steady operation will be conducted. As several authors have pointed out that the use of scale-resolving methods might result in better agreement of the velocity field, PANS and ILES approaches will also be evaluated for steady operation. The simulations will be compared to experimental results of Trivedi et al. [38] using velocity fields, pressure measurements and integral quantities. The main focus of the turbulence modelling comparison will be towards the flow field features and velocity profiles of the different models. The intention of the steady operation part is to contribute to an increased insight in the use of scale-resolving models applied to high-head Francis turbines. Simulations at transient operation will be performed by application of a flow-driven rotational mesh motion class on the Francis-99 turbine. For this case the aim is to prove that FOAM-extend can be used for simulation of changing operating conditions by investigation of the dynamic state of the runner and pressure data during the initial transient.

To limit the scope of the project, the steady operation at part load and high load will not be studied. The effects of seals, bearings, leakage flow or other frictional influences will not be investigated, nor accounted for. Further will no re-meshing or morphing of the mesh for the transient operation, such as moving guide vanes, be performed.

In summary, there are two main goals of this thesis. Firstly, the performance of current URANS turbulence models and scale-resolving models is to be evaluated and compared. Secondly, a flow-driven mesh rotation implementation is to be applied to a transient operation flow scenario.

1.4 Hydroelectric turbines

Hydroelectric power plants extract power from the potential energy of stored water using a turbine. A turbine consists of a penstock, spiral casing, stay vanes, guide vanes, runner, generator and a draft tube. The penstock is the pipe leading from the reservoir to the spiral casing inlet. The spiral casing have a decreasing cross-sectional area and is used to distribute the water evenly across the radial inlet through the stay vanes which is structural elements keeping the mechanical integrity of the spiral casing intact. The guide vanes are used to induce a swirl into the runner and also to regulate how much water is going through the turbine. The runner is the rotating part which is connected to a generator that produces power. The runner extracts power from the water by reducing the swirl created by the guide vanes and the in an ideal case the flow out of the runner into the draft tube will be completely axial. The draft tube then leads the water downstream to the river while the pressure is recovered.

There are three different types of turbines in extensive use for power generation today. There is the Pelton turbine, which is an impulse turbine where jets of water is driving the runner. This type of turbine is operated at high heads and low flow rates. There is also the Kaplan turbine, which can be seen as a propeller spinning the opposite direction, extracting work from the flow. Kaplan turbines typically operate at low heads and high flow rates, like most of the Swedish rivers. The third type is the Francis turbine, which has a wide operation span in between the Pelton and Kaplan machines. Both Francis and Kaplan turbines are reaction turbines, driven by the pressure difference of the runner blades. The Francis turbine can be used for both low and high heads depending on design.

The increased amount of intermittent energy production means that the hydroelectric plants need to be operated at part load. This is regulated by decreasing the angle of the guide vanes to limit the flow rate through the machine. At high load the guide vanes are opened to allow for a higher flow rate. There are also situations when sudden changes in the operating conditions are needed. A load-rejection condition includes running at stable operating condition (often BEP) then the generator is suddenly disconnected from the turbine, leading to pressure variations in the turbine and a high increase in the runner rotational speed. The guide vanes are slowly closed during the process to protect the turbine from damage due to high runner rotational speeds. If the guide vanes are closed too quickly the risk of severe pressure pulsations in the penstock increases.

1.4.1 The Francis-99 turbine

The Francis-99 turbine, located at NTNU, is a scale model of a prototype turbine at the Tokke power plant in Norway. It is a high-head Francis turbine consisting of 30 runner blades of which fifteen are splitter blades of half length. In the distributor there are 14 stay vanes and 28 guide vanes. The prototype and model data can be seen in table 1.1. The test rig illustrated in figure 1.1 consists of an upstream pressure tank with a pipe that leads to the distributor inlet, through the turbine and to the downstream tank. The data for the three operating conditions can be seen in table 1.2, along with the uncertainty of the measurements. These data are used for setting up simulations and comparing results.

	Scale	H [m]	P [kW]	D [m]
Prototype	-	377	110×10^3	1.779
Model	1:5.1	12	22	0.349

Table 1.1: Prototype and model turbine comparison.

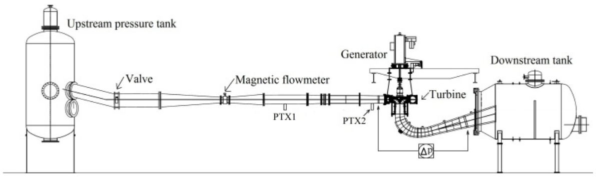

Figure 1.1: *The Francis-99 test rig.*

Table 1.2: Experimental operating points

Parameter	Symbol	Part load	BEP	Full load	Uncertainty
Net head [m]	H	12.29	11.91	11.84	0.05%
Flow rate [m^3/s]	Q	0.071	0.203	0.221	0.1%
Runner frequency [Hz]	f	6.77	5.59	6.16	0.05%
Guide vane angle [°]	α	3.91	9.84	12.44	0.044°
Efficiency [%]	η_M	71.69	92.61	90.66	0.16%
Torque [N m]	T	137.52	619.56	597.99	0.034%
Friction torque [N m]	T_{LM}	6.54	8.85	7.63	0.052%
Differential pressure [kPa]	Δp	120.394	114.978	114.033	0.018%
Inlet pressure [kPa]	p_1	219.93	216.54	210.01	0.05%
Density [kg/m^3]	ρ	999.23	999.19	999.20	0.01%
Kinematic viscosity [10^{-7} m^2/s]	ν	9.57	9.57	9.57	-

2 Theory

2.1 Hydrodynamic definitions

The characteristics and performance of a hydroelectric turbine can be characterised by some key numbers. The head is the total pressure difference between the runner inlet and outlet measured in metres,

$$H = \frac{\Delta p_0}{\rho g}, \tag{2.1}$$

where Δp_0 is the difference in total pressure defined

$$\Delta p_0 = \Delta p + \frac{1}{2}\rho\left(U_{in}^2 - U_{out}^2\right), \tag{2.2}$$

by the workshop organisers, slightly different than the established IEC norm,

$$\Delta p_0 = \Delta p + \frac{1}{2}\rho\left(U_{in}^2 - U_{out}^2\right) + \rho g \Delta z. \tag{2.3}$$

where ρ is the free-stream density, U_{in} and U_{out} is the inlet and outlet velocity, respectively, g is the gravitational acceleration and Δz is the height difference between inlet and outlet. In the Francis-99 model the gravitational term amounts to about 4.5 % of the total pressure difference. The hydraulic efficiency is one of the most important performance indicators, defined as

$$\eta_h = \frac{T\omega}{\Delta p_0 Q}. \tag{2.4}$$

T is the torque affecting the outgoing turbine shaft, ω is the angular velocity and Q is the volumetric flow rate. The maximum available work in a turbine is determined by the difference in total pressure before and after the runner. By using equation 2.1 the potential work output can be written

$$\Delta W_{th} = gH_E = \frac{p_{02} - p_{03}}{\rho}, \tag{2.5}$$

where station 2 is the runner inlet and station 3 is the runner outlet. There are however always losses in a turbine, and the useful work extracted from a turbine can be approximated with Euler's turbine equation, defined by Dixon and Hall [8] as

$$\Delta W = U_2 c_{\theta 2} - U_3 c_{\theta 3} = \omega\left(r_2 c_{\theta 2} - r_3 c_{\theta 3}\right). \tag{2.6}$$

If all available work is translated into rotation, meaning there are no torque braking the runner, a relation for the maximum attainable speed can be expressed as a combination of equations 2.5 and 2.6 as

$$\omega_{max} = \frac{\Delta W_{th}}{\left(r_2 c_{\theta 2} - r_3 c_{\theta 3}\right)} = \frac{\Delta p_0}{\rho\left(r_2 c_{\theta 2} - r_3 c_{\theta 3}\right)}, \tag{2.7}$$

where r_3 is defined as

$$r_3 = \sqrt{r_{3,tip}^2 - r_{3,hub}^2}. \tag{2.8}$$

This relation can be used to get an idea of the runaway speed of a turbine for a given head or total pressure difference.

2.2 Governing equations

The most common approach to CFD is to solve the Navier-Stokes equations on a discretised grid as a representation of the geometry using the finite volume method. The incompressible Navier-Stokes equations in conservative form with body forces neglected read

$$\frac{\partial u_i}{\partial x_i} = 0 \tag{2.9}$$

$$\frac{\partial u_i}{\partial t} + \frac{\partial u_i u_j}{\partial x_j} = -\frac{1}{\rho}\frac{\partial p}{\partial x_i} + \nu\frac{\partial^2 u_i}{\partial x_j^2}. \tag{2.10}$$

Equations 2.9 and 2.10 are the continuity and momentum equations, respectively. These equations can predict the pressure and velocity field in a region with high accuracy. The computational time it takes to solve the Navier-Stokes equations on an arbitrary industrial problem is, however, prohibitively large for current generation computers. This is due to the large scale separation between the flow domain and the the smallest, dissipative scales, which can be in the order of micrometres or even nanometres while the domain can be several metres large. As the resolution need to be in the order of the dissipative eddies in DNS, the domain may require trillions of elements, which cannot yet be handled.

2.2.1 Turbulence modelling

The inability to solve the Navier-Stokes equations for turbulent flows have led to countless attempts to model some of, or all of the turbulent fluctuations in using either LES (Large Eddy Simulation) or RANS (Reynolds Averaged Navier-Stokes). In RANS all the velocity fluctuations are modelled while in LES only the scales smaller than the grid size are modelled. The RANS equations are written

$$\frac{\partial \bar{u}_i \bar{u}_j}{\partial x_j} = -\frac{1}{\rho}\frac{\partial \bar{p}}{\partial x_i} + \frac{\partial}{\partial x_j}\left(\nu\frac{\partial \bar{u}_i}{\partial x_j} - \overline{u_i' u_j'}\right). \tag{2.11}$$

The last term, $-\overline{u_i' u_j'}$ is called the Reynolds stress tensor. This is the term that poses the problem in the RANS modelling approach as it is unknown and needs to be modelled. In RSM (Reynolds stress modelling) one transport equation for each of the tensor components is solved resulting in six extra equations to solve, as the tensor is symmetric. The main advantage of this model is that the production of turbulence is solved for and not modelled, meaning it is much more sensitive to curvature effects, buoyancy and other anisotropic effects. The problem is the high cost to solve these equations compared to a two-equation model. There have been some development in trying to keep the anisotropy but decrease the computational demand of the RSM by a number of methods such as the EARSM of Wallin [40] and the SSG model of Speziale, Sarkar, and Gatski [34].

Another way to model the Reynold's stresses, which is the most common method, is to use Boussinesq's assumption, that $-\overline{u_i' u_j'}$ can be approximated with a turbulent viscosity, to add to the laplacian term in the Navier-Stokes equations. Boussinesq's assumption states that the Reynolds stress tensor is proportional to trace-less mean strain rate tensor and can be written

$$-\overline{u_i' u_j'} = 2\nu_t S_{ij} - \frac{2}{3}k\delta_{ij} = \nu_t\left(\frac{\partial \bar{u}_i}{\partial x_j} + \frac{\partial \bar{u}_j}{\partial x_i}\right) - \frac{2}{3}k\delta_{ij} \tag{2.12}$$

for incompressible flow, where δ_{ij} is the Kronecker delta. The RANS equations with the turbulent viscosity approximation reads

$$\frac{\partial \bar{u}_i \bar{u}_j}{\partial x_j} = -\frac{1}{\rho}\frac{\partial \bar{p}}{\partial x_i} + \frac{\partial}{\partial x_j}\left((\nu + \nu_t)\frac{\partial \bar{u}_i}{\partial x_j}\right). \tag{2.13}$$

In eddy viscosity based turbulence models the common goal is to predict the value of ν_t as accurately as possible. This is a difficult task as turbulence is almost always highly anisotropic, which the scalar ν_t cannot account for. This deficiency have been the focus of research in turbulence modelling in recent years with the introduction of VR models, which combines the high accuracy of resolving models while keeping the computational cost to a realisable level. This is done by filtering of the velocity field, trying to resolve the large, anisotropic scales and model the small, isotropic scales.

The traditional VR model is LES, in which all scales larger than the grid resolution are resolved and those smaller than the grid size are modelled using a so called sub-grid model. As only the smallest scales are modelled the selection of turbulence model has a smaller impact on the solution than for a RANS model, and the isotropy assumption is also more valid for small eddies. The downside with LES is that the filtering width, and hence the grid resolution needs to be in the inertial sub-range of the turbulent spectrum. This might not pose a problem in the centre of the flow but at the walls this resolution becomes very fine, and often prohibits the use of LES in most practical applications. An increasingly popular method is ILES, where no explicit sub-grid scale model is used but the discretisation method is chosen in a manner that the numerical diffusion replaces the sub-grid model implicitly, hence *implicit* LES. This is a pragmatic approach to turbulence modelling rather than a theoretical one, focusing on results rather than mathematical principles. Some research have however been performed on the physicality of the discretisation methods by Grinstein and Fureby [13].

To combine the high accuracy of the LES method while keeping the computational requirements closer to those of URANS methods several models have emerged, such as DES, VLES, PANS and ZLES. In DES the sub grid viscosity is explicitly increased close to the walls to account for the decrease in resolved turbulence. VLES is an LES simulation with a coarser grid than a true LES, resulting in the grid size being above that of the inertial sub-range scales. PANS is derived as a partially resolved, partially modelled approach with no explicit filtering width applied. Instead coefficients are used to define the ratio of modelled scales to all scales.

2.2.2 k-ε RNG

The most commonly used two-equation closure model is the k-ε model. Despite its popularity the k-ε model has some severe weaknesses, as it needs wall-functions and is often unable to capture recirculating flow. Because of this, many improved versions have been developed to mitigate the problems with the model. One such improvement is the re-normalisation group, RNG, k-ε model of Yakhot et al. [41]. It accounts for the effects of a wider range of motion affecting the turbulent diffusion, rather than the single scale in the standard k-ε model. The governing equations in incompressible form are

$$\nu_t = C_\mu \frac{k^2}{\varepsilon} \tag{2.14}$$

$$\frac{\partial k}{\partial t} + \bar{u}_j \frac{\partial k}{\partial x_j} = \frac{\partial}{\partial x_j}\left[\left(\nu + \frac{\nu_t}{\sigma_{ku}}\right)\frac{\partial k}{\partial x_j}\right] + P_k - \varepsilon \tag{2.15}$$

$$\frac{\partial \varepsilon}{\partial t} + \bar{u}_j \frac{\partial \varepsilon}{\partial x_j} = \frac{\partial}{\partial x_j}\left[\left(\nu + \frac{\nu_t}{\sigma_{\varepsilon u}}\right)\frac{\partial \varepsilon}{\partial x_j}\right] + C_{\varepsilon 1} P_k \frac{\varepsilon}{k} - C^*_{\varepsilon 2}\frac{\varepsilon^2}{k}, \tag{2.16}$$

where

$$C^*_{\varepsilon 2} = C_{2\varepsilon} + \frac{C_\mu \eta^3 (1 - \eta/\eta_0)}{1 + \beta\eta^3} \tag{2.17}$$

$$\eta = S\frac{k}{\varepsilon} \tag{2.18}$$

$$P_k = \nu_t S^2 \tag{2.19}$$

$$S = \sqrt{2 S_{ij} S_{ij}} \tag{2.20}$$

$$S_{ij} = \frac{1}{2}\left(\frac{\partial \bar{u}_i}{\partial x_j} + \frac{\partial \bar{u}_j}{\partial x_i}\right). \tag{2.21}$$

2.2.3 k-ω SST

A newer and higher fidelity model that is commonly used in turbomachinery is the k-ω Shear Stress Transport model of Menter [23]. It uses a transformed version of the k-ε model far from the walls and the k-ω model close to the walls, combining the strength of the two models. Blending functions are used to transition from the ω coefficients close to the wall to the ε coefficients in the free stream. The governing equations are

$$\nu_t = \frac{a_1 k}{max(a_1\omega, SF_2)} \tag{2.22}$$

$$\frac{\partial k}{\partial t} + \bar{u}_j \frac{\partial k}{\partial x_j} = \frac{\partial}{\partial x_j}\left[\left(\nu + \frac{\nu_t}{\sigma_k}\right)\frac{\partial k}{\partial x_j}\right] + P_k - \beta^* k\omega \tag{2.23}$$

$$\frac{\partial \omega}{\partial t} + \bar{u}_j \frac{\partial \omega}{\partial x_j} = \frac{\partial}{\partial x_j}\left[\left(\nu + \frac{\nu_t}{\sigma_\omega}\right)\frac{\partial \omega}{\partial x_j}\right] + \frac{\gamma}{\nu_t} P_k - \beta\omega^2 + 2(1 - F_1)\frac{\sigma_{\omega 2}}{\omega}\frac{\partial k}{\partial x_j}\frac{\partial \omega}{\partial x_j}, \tag{2.24}$$

with blending functions

$$F_1 = \tanh\left[\left(min\left[max\left(\frac{\sqrt{k}}{\beta^*\omega y}, \frac{500\nu}{y^2\omega}\right), \frac{4\sigma_{\omega 2}k}{CD_{k\omega}y^2}\right]\right)^4\right] \tag{2.25}$$

$$F_2 = \tanh\left[\left(max\left(\frac{2\sqrt{k}}{\beta^*\omega y}, \frac{500\nu}{y^2\omega}\right)\right)^2\right] \tag{2.26}$$

$$CD_{k\omega} = max\left(2\rho\sigma_{\omega 2}\frac{1}{\omega}\frac{\partial k}{\partial x_j}\frac{\partial \omega}{\partial x_j}, 10^{-10}\right). \tag{2.27}$$

The production is formulated using a limiter of ten times the destruction term

$$P_k = min\left(\nu_t S^2, 10\beta^*\omega k\right). \tag{2.28}$$

2.2.4 k-ω SST PANS

The motivation for the numerous hybrid LES-RANS models that have emerged recently is to have an accuracy close to that of an LES method with requirements close to that of URANS simulations. The first hybrid methods suggested were Hybrid LES/RANS by Speziale [33] and DES by Spalart and Shur [32]. These have later been modified and further developed by many authors. The PANS method first proposed by Girimaji [10] is a filtered URANS model that uses factors to switch between modelled and resolved equations. The present formulation of the PANS model is based on the k-ω SST URANS model. The formulation used in this work is that of Lakshmipathy and Togiti [20], written

$$\nu_t = \frac{a_1 k_u}{max(a_1\omega_u, SF_2)} \tag{2.29}$$

$$\frac{\partial k_u}{\partial t} + \bar{v}_j\frac{\partial k_u}{\partial x_j} = \frac{\partial}{\partial x_j}\left[\left(\nu + \frac{\nu_t}{\sigma_{ku}}\right)\frac{\partial k_u}{\partial x_j}\right] + P_{ku} - \beta^* k_u\omega_u \tag{2.30}$$

$$\frac{\partial \omega_u}{\partial t} + \bar{v}_j\frac{\partial \omega_u}{\partial x_j} = \frac{\partial}{\partial x_j}\left[\left(\nu + \frac{\nu_t}{\sigma_{\omega u}}\right)\frac{\partial \omega_u}{\partial x_j}\right] + \frac{\gamma}{\nu_t}P_{ku} - \beta'\omega_u^2 + 2(1-F_1)\frac{\sigma_{\omega 2u}}{\omega_u}\frac{\partial k_u}{\partial x_j}\frac{\partial \omega_u}{\partial x_j} \tag{2.31}$$

$$\beta' = \gamma\beta^* - \frac{\gamma\beta^*}{f_\omega} + \frac{\beta}{f_\omega} \qquad f_\omega = \frac{\omega_u}{\omega} = \frac{f_\varepsilon}{f_k}. \tag{2.32}$$

The blending functions and coefficients are the same as in the SST model and the unresolved turbulent Prantl numbers are defined using the zero transport theorem, valid for high-Re flows as

$$\sigma_{ku} = \sigma_k\frac{f_k}{f_\omega} \qquad \sigma_{\omega u} = \sigma_\omega\frac{f_k}{f_\omega}. \tag{2.33}$$

Formulation of f_k

The filtering of the PANS model is governed by the ratios of unresolved-to-total kinetic energy and dissipation, f_k and f_ε. The selection of these parameters is arguably the most critical part of a PANS simulation as it will have a direct impact on the amount of resolved velocity scales. A value of f_k equal to unity means that the unsteady RANS equations are solved, while a f_k of zero means that the full Navier-Stokes equations are solved. There are a number of different ways to choose f_k, a fixed, uniform value being the traditional route. In previous studies values of f_k around 0.4 have shown good results [7]. The computational grid can however support different values of f_k at different locations and several suggestions have been made to calculate the value of f_k based on the turbulence energy spectrum reasoning. One way of using a variable f_k is presented by Girimaji and Abdol-Hamid [11] using Kolmogorov reasoning like the grid spacing for DNS simulations but for the resolved scales in the PANS method. The smallest resolved length scale can be expressed as

$$\eta_r \approx \left(\frac{\nu_u^3}{\varepsilon}\right)^{1/4}, \tag{2.34}$$

where ν_u is the unresolved eddy viscosity. In moderate to high Reynolds flows the dissipative scales can be assumed to be much smaller than the resolved scales and f_ε=1, meaning $\varepsilon_u = \varepsilon$. We then have

$$\nu_u = C_\mu \frac{k_u^2}{\varepsilon_u} \approx C_\mu f_k^2 \frac{k^2}{\varepsilon} \tag{2.35}$$

and by introducing the Taylor length scale $\Lambda = \frac{k^{3/2}}{\varepsilon}$ and setting the smallest resolved scale to be greater or equal to the grid dimension, $\eta_r \geq \Delta$ the minimum modelling a grid can support is

$$f_k \geq \frac{1}{\sqrt{C_\mu}} \left(\frac{\Delta}{\Lambda}\right)^{2/3}. \tag{2.36}$$

This formulation is originally used with $\Delta = min\,(\Delta x, \Delta y, \Delta z)$, but $\Delta = (\Delta x \Delta y \Delta z)^{1/3}$ can also be used. Davidson [7] found that for coarse grids the value of f_k by using equation 2.36 is much larger than the calculated value k_u/k leading to a too high turbulent viscosity effectively killing the resolved turbulence. Another downside with using equation 2.36 is that boundedness between 0 and 1 is not ensured, especially when $\Delta \approx \Lambda$ f_k may be larger than unity. This problem can however be removed by explicitly introducing a limiter. Recently, a new formulation of f_k has been proposed by Foroutan and Yavuzkurt [9] to mitigate the problems of the previous formulation. The reasoning behind this new formulation originates in spectral analysis of the turbulence energy spectrum shown in figure 2.1. Assuming the cut-off wave number is defined as $\kappa_c = \pi/\Delta$ the total, and unresolved kinetic energy, k and k_u can be expressed as

$$k = \int_0^\infty E(\kappa)d\kappa \tag{2.37}$$

$$k_u = \int_{\kappa_c}^\infty E(\kappa)d\kappa \tag{2.38}$$

respectively. The ratio of unresolved to total kinetic energy, f_k can then be written as

$$f_k = \frac{k_u}{k} = 1 - \frac{\int_{\kappa_c}^\infty E(\kappa)d\kappa}{\int_0^\infty E(\kappa)d\kappa}. \tag{2.39}$$

A Von Kármán energy spectrum equation is then used to obtain a formula for f_k

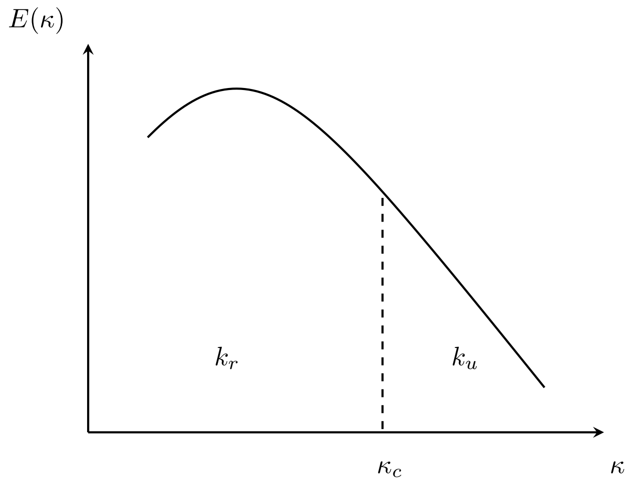

Figure 2.1: *Turbulence kinetic energy spectrum showing the modelling cut-off wave number, κ_c.*

$$E(\kappa) = C_k \varepsilon^{2/3} \kappa^s \left[\left(\frac{C_k \varepsilon^{2/3}}{C_s} \right)^{\frac{2}{5+3s}} + \kappa^{2/3} \right]^{-\frac{5+3s}{2}} \tag{2.40}$$

By combining equations 2.39 and 2.40 choosing constants C_k=1.5 and s=2 the final formulation of f_k becomes

$$f_k = 1 - \left[\frac{\left(\frac{\Lambda}{\Delta}\right)^{2/3}}{0.23 + \left(\frac{\Lambda}{\Delta}\right)^{2/3}}\right]^{9/2} . \tag{2.41}$$

The turbulence and grid length scales are calculated as before,

$$\Lambda = \frac{k^{3/2}}{\varepsilon} \tag{2.42}$$

$$\Delta = (\Delta x \Delta y \Delta z)^{1/3} . \tag{2.43}$$

The difference between equations 2.41 and 2.36 is that the former is valid in the full range of wave numbers and not only in the inertial range. Foroutan and Yavuzkurt [9] use a precursor RANS simulation to calculate the average Taylor length scale and f_k is then calculated and fixed in time. This is the most common way to formulate a spatially variable value of f_k, for reasons of stability and simplicity. The value of f_k can also be calculated using a dynamic approach, similar to a dynamic Smagorinsky LES, as Basara, Krajnović, and Girimaji [2] did, where f_k was updated every time-step using equation 2.36. It should be noted that when f_k varies in time and space commutation errors arise with the current PANS formulation. The modifications needed to account for these errors are presented in [12].

2.2.5 Implicit LES

In explicit LES the Navier-Stokes equations are filtered to resolve the turbulent fluctuations larger than the grid size, Δx. The smaller scales are modelled using a sub-grid scale (SGS) viscosity, similar to the modelling of the RANS eddy viscosity. The assumption of isotropy holds much better for the SGS scales as only the smallest scales are modelled. To illustrate the idea behind ILES the discretisation of the function $\phi(x)$ is shown in figure 2.2. Using a Taylor series development at the point E

$$\phi_E = \phi_P + \left(\frac{\partial \phi}{\partial x}\right)_P \Delta x + \left(\frac{\partial^2 \phi}{\partial x^2}\right)_P \Delta x^2 + ..., \tag{2.44}$$

the gradient at point P may be evaluated by re-arrangement of the terms as

$$\left(\frac{\partial \phi}{\partial x}\right)_P = \frac{\phi_E - \phi_P}{\Delta x} + \mathcal{O}(\Delta x). \tag{2.45}$$

This is called a forward difference approximation of the gradient of ϕ at point P. The truncated terms, $\mathcal{O}(\Delta x)$

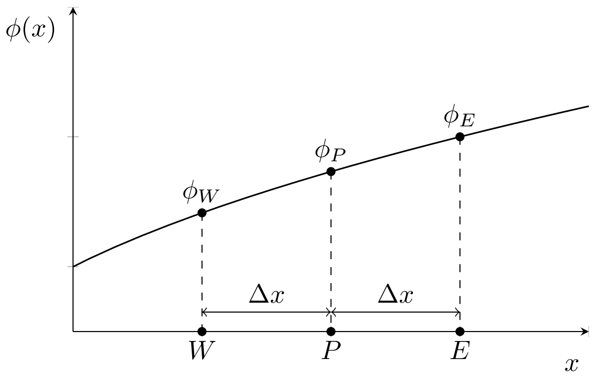

Figure 2.2: *The discretisation of an arbitrary function ϕ with grid points P (point), W (west) and E (east).*

are then neglected, creating an error proportional to the order of the neglected terms, in this simple case first order. This is the discretisation error, giving rise to dissipative effects, whih can be described as an artificial numeric viscosity, ν_{num}. The motivation of the ILES method is that because of the SGS viscosity being very small, it can be in the same order of the numerical viscosity, ν_{num}. By introducing "smart" schemes that adapt to the flow and give the right amount of numerical dissipation the explicit SGS model is not needed. The development of such schemes in addition to validation is currently the main research subject of the ILES method.

2.3 Rotordynamics

The state of motion of a body affected by exterior forces, $f(t)$, is written

$$I\alpha(t) + J\omega(t) + K\theta(t) = f(t) \tag{2.46}$$

with θ, ω and α being the angular rotation, speed and acceleration about the axis of rotation. It is assumed here that all degrees of freedom except the rotation about the runner axis are fixed, and that $J \approx K \approx 0$. The rotation of the turbine runner is a consequence of the pressure and viscous forces of the water flowing through the turbine. To determine the rigid body motion of the runner a balance of moments about the rotational axis can be expressed as

$$\sum T = \alpha \sum I \tag{2.47}$$

where $\sum T$ is the sum of all torques about the axis, α is the angular acceleration about the axis and $\sum I$ is the sum of polar moments of inertia of the rotating parts. Depending on the level of complexity of the experiment or simulation the total torque and the total moment of inertia can consist of a number of terms. Some examples of terms can be

$$T_{shaft} + T_{pressure} + T_{viscous} + T_{leakage} = \alpha\left(I_{runner} + I_{generator} + I_{water}\right). \tag{2.48}$$

From this equation the angular acceleration is obtained

$$\alpha = \frac{d\omega}{dt}, \tag{2.49}$$

and the angular speed can be calculated by separating the variables

$$\Delta\omega = \int_{\Delta t} \alpha(t) dt. \tag{2.50}$$

The largest contributions to the total torque in the current application are the shaft torque and the hydraulic torque. The shaft torque, T_{shaft}, extracts the energy from the rotating runner to the generator, which provides the electric grid with power. The hydraulic torque, T_h can be calculated by integrating the pressure and shear stress over the rotating parts and projecting it on an axis perpendicular to that of the runner rotation axis. In mathematical terms it can be expressed as

$$T_h = -\int_A \mathbf{r} \times (p\, \mathbf{e}_N) dA + \int_A \mathbf{r} \times (\tau_w \mathbf{e}_T) dA, \tag{2.51}$$

where $\mathbf{e}_N$ is the face normal unit vector and $\mathbf{e}_T$ is the face tangential vector, $\mathbf{r}$ is the vector from the axis of rotation to the face centre, A is the region on which the hydraulic forces are applied and dA is the area of each infinitesimal face of that region.

3 Method

3.1 Geometry and Grid generation

The turbine geometry used is the same as the one provided by the Francis-99 workshop organisers. It consists of three domains all meshed separately: the distributor, the runner and the draft tube. An overview of the geometry is shown in figure 3.1. The Francis-99 mesh provided by the workshop was of insufficient quality and

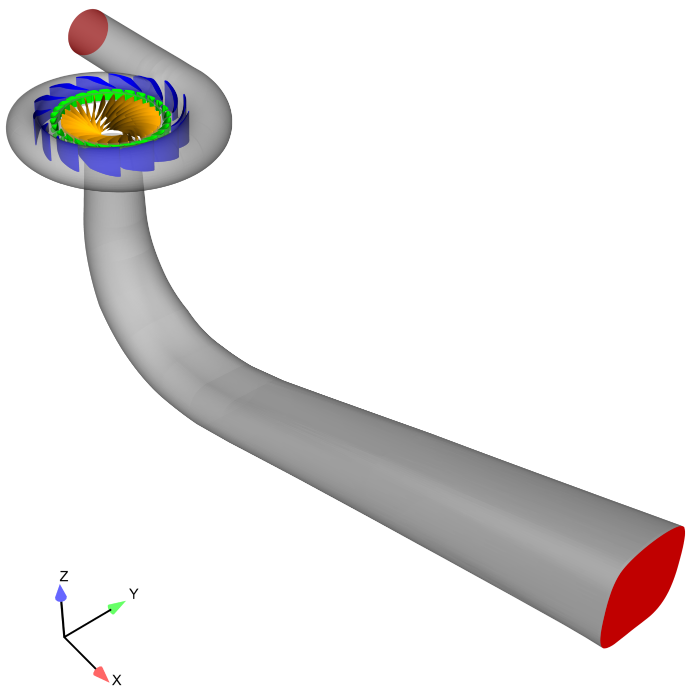

Figure 3.1: *The Francis-99 geometry with the inlet and outlet in red, stay vanes are blue, guide vanes green and the runner is orange.*

was improved by Stoessel [35], but further improvements were possible. The largest potential for improvement was assessed to be the interface between the runner and the draft tube as the quality of the GGI interpolation was likely to be affected by the size matching of the grid spacing on each side of the interface. The grid resolution in the draft tube was therefore increased in the axial and radial direction. This change also brings down the wall spacing of the runner hub end cap. The overall resolution in the upper part of the draft tube was increased while the part closest to the outlet was coarsened for a net reduction of cells in the draft tube. In figure 3.2 the part of the region of comparison is visualised by a black frame.

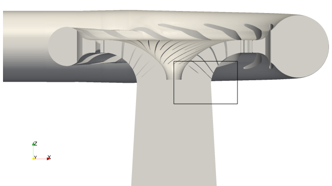

Figure 3.2: *Runner-draft tube GGI interface comparison*

Region	Cells ($\times 10^6$)
Spiral casing	3.53
Runner	7.48
Draft tube	3.35
Total	14.36

Table 3.1: Mesh cell count

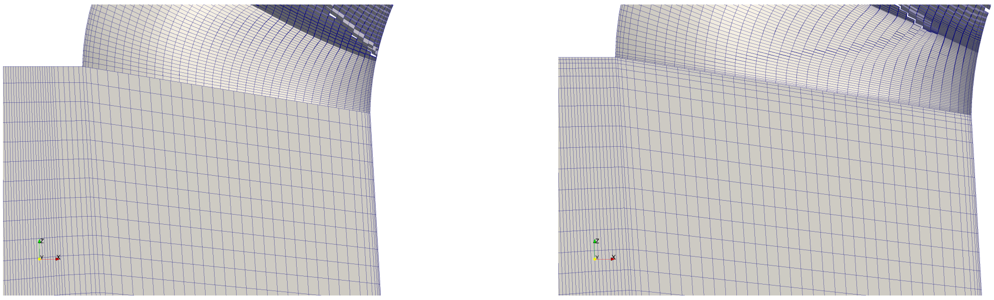

(a) *Old mesh* (b) *New mesh*

Figure 3.3: *Improvement of the GGI-interface grid size matching*

Another important region with high probability of sharp gradients is the trailing edge of the blade. Both the wall spacing, resolution and volume ratio of the old mesh was inadequate at the main blade trailing edge, the improvements can be seen in figure figure 3.4. The wall spacings of the splitter blade, particularly at the trailing edge, were reduced to increase the resolution at that location. This refinement can be seen in figure 3.5. The overall mesh resolution increase in the runner resulted in a 65 % cell count increase for a total of 7.48 million cells. The spiral casing mesh was judged to be of adequate quality due to its small influence on the draft tube flow field, and no modifications were made. All mesh modifications combined resulted in a total cell count of 14.36 million cells, an increase of 18 %, the mesh count for all regions can be seen in table 3.1. No large changes were made to the wall spacings, and the y^+ values were mostly in the wall function range as can be seen in figure 3.6. The presented values are from the k-ω SST model simulation.

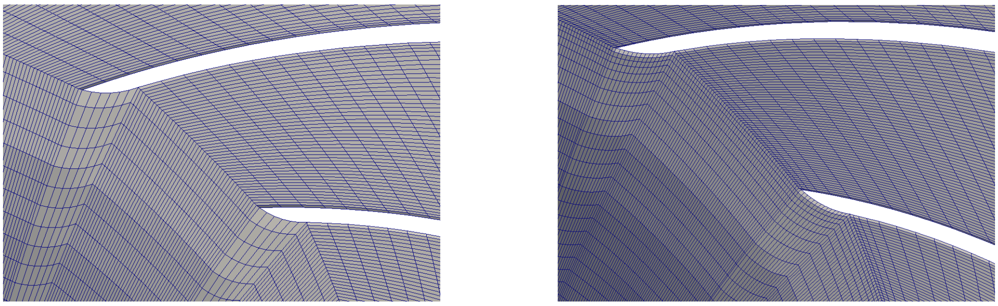

(a) *Old mesh* (b) *New mesh*

Figure 3.4: *Improvement of the main blade trailing edge wall spacing, resolution and volume ratio.*

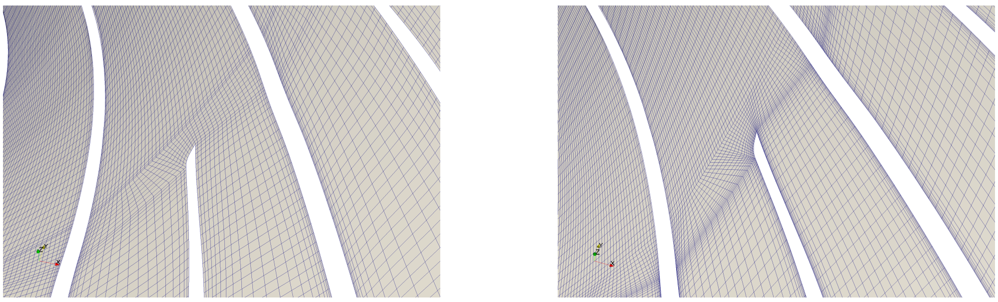

(a) *Old mesh* (b) *New mesh*

Figure 3.5: *Improvement of the splitter blade trailing edge wall spacing.*

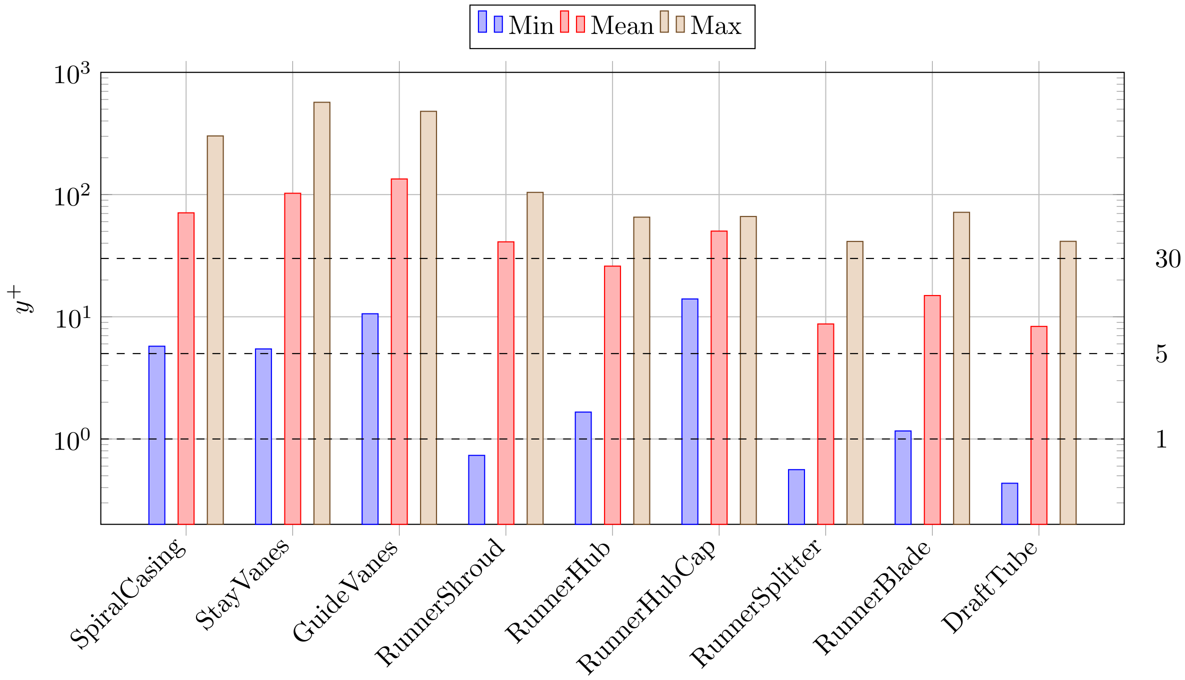

Figure 3.6: *Values of y^+ for the k-ω SST model at the wall boundaries.*

3.2 Simulation setup

The focus of the simulations was mainly on the BEP operating condition, because of the deviations in the draft tube velocity profiles in many of the 2014 workshop papers. A load-rejection simulation was performed to create understanding and develop methods for the relatively unknown transient operation cases. In the steady BEP simulations the k-ε RNG, k-ω SST, k-ω SST PANS and ILES turbulence models were compared. In the load-rejection simulations the ILES model was used to enhance the capturing of transient phenomena. The simulation was initially run with a constant resistance torque on the runner shaft representing the generator. The moment of inertia of the system was estimated as

$$I = I_{runner} + I_{water} + I_{generator}, \tag{3.1}$$

where the contributions from the runner and water was evaluated in Catia V5R19, and the contribution from the generator was chosen arbitrarily as $I_{generator} = I_{runner} + I_{water}$. The torque was then removed and the moment of inertia corresponding to the generator was removed to account for the de-coupling of the generator. The simulation was run for a duration of 0.15 s during which the inlet flow rate was held constant. This corresponds to a displacement pump being able to feed the turbine with a constant volumetric flow rate regardless of the runner angular velocity. This is not the case for the experimental equipment but it was done as an approximation to enable simpler boundary conditions to be used.

3.2.1 Solver settings

FOAM-extend 3.1 was used to solve the governing equations using the incompressible transient solver *transientSimpleDyMFoam*. It is based on the SIMPLE algorithm for the pressure-velocity coupling and supports moving meshes. To solve the pressure correction equation the PCG algorithm was chosen over the often faster GAMG algorithm because of the increased performance on large clusters with many cores. The low under-relaxation factors of the turbulent quantities was needed for stability, and as transientSimpleDyMFoam solves the turbulence equations every corrector loop the evolution of turbulence was judged to be sufficient. The solver settings for all simulations are presented in table 3.2.

Table 3.2: Solver settings

Variable	Solver	Preconditioner	Absolute tolerance	Relative tolerance	Under-relaxation factor
p	PCG	DIC	10^{-5}	0.01	0.3
U	PBiCG	DILU	10^{-7}	0	0.6
k	PBiCG	DILU	10^{-7}	0	0.2
ε	PBiCG	DILU	10^{-7}	0	0.2
ω	PBiCG	DILU	10^{-7}	0	0.2

3.2.2 Discretisation

First and second order schemes were used in the discretisation of the governing equations. The momentum divergence term was discretised using the second order *linearUpwind* scheme, which is a combination of the linear and the upwind schemes. The turbulence terms were discretised using a first order upwind scheme for the sake of stability. For the temporal terms the first order Euler scheme was used, also for stability. The use of the first order schemes is not optimal, particularly for the temporal terms as it can cause a level of temporal diffusion that is too high, particularly for scale-resolving turbulence models. This was somewhat mitigated by the use of a relatively small time step of 1.6564×10^{-4} s which corresponds to 0.33° per time step. It should be noted that the ILES simulation was not planned from the start, but was the result of an error in the implementation in another turbulence model. This error resulted in zero eddy viscosity in the whole region, effectively making in an implicit LES simulation. This is the reason for the RANS-like discretisation schemes begin used.

3.2.3 Boundary Conditions

The guide vane-runner and runner-draft tube interfaces were handled by the use of GGI interpolation. The remaining boundary conditions are presented in table 3.3. Note that it is the kinematic pressure, $P = p/\rho$ [$\mathrm{m}^2/\mathrm{s}^2$], that is solved for as in all incompressible solvers in FOAM-extend. The inlet boundary condition *timeVaryingFlowRateInletVelocity* was used to ramp the flow rate together with the runner rotational speed and was then kept constant.

General Grid Interface

The GGI interface method, developed for FOAM-extend primarily by Beaudoin and Jasak [3], was used to couple the stationary and rotating regions. Two GGI interfaces were therefore needed, shown in figure 3.7. GGI interpolation is a method for coupling variable values between non-conformal patches often used in simulations of rotating parts to couple the static and rotating regions. There are some important requirements that have to be addressed however; the mesh resolution in the direction normal to the interface should be matched as closely as possible between the neighbouring patches. Great care should also be taken when creating the geometry of the interfaces to ensure matching geometry.

Turbulence inlet boundary conditions

To calculate the inlet boundary conditions for the turbulence quantities the following relations were used. The turbulence kinetic energy was calculated as

$$k = \frac{3}{2}\left(UI\right)^2, \tag{3.2}$$

where the turbulence intensity $I = u'/U$ was chosen arbitrarily to 7%. The ratio of eddy viscosity to fluid viscosity was selected by rule of thumb as $\beta = \frac{\nu_t}{\nu} = 10$. The turbulence dissipation rate and the specific

Table 3.3: Boundary conditions BEP operating condition

Variable	Boundary	Turbulence Models	Type	Value
U				m/s
	Inlet	All	timeVaryingFlowRateInletVelocity	$Q = 0.203\,\mathrm{m}^3/\mathrm{s}$
	Outlet	All	zeroGradient	-
	Spiral casing walls	All	fixedValue	U=0
	Runner walls	All	movingWalls	U_{rel}=0
	Draft tube walls	All	fixedValue	U=0
P				$\mathrm{m}^2/\mathrm{s}^2$
	Inlet	All	zeroGradient	-
	Outlet	All	fixedValue	0
	Walls	All	zeroGradient	-
ν_t				m^2/s
	Inlet	RNG	calculated	-
	Outlet	RNG	zeroGradient	-
	Walls	RNG	nutSpaldingWallFunction	-
k				$\mathrm{m}^2/\mathrm{s}^2$
	Inlet	All	fixedValue	0.0408
	Outlet	All	zeroGradient	-
	Walls	RNG SST PANS	kqRwallfunction	-
		ILES	zeroGradient	-
ω				1/s
	Inlet	SST PANS ILES	fixedValue	4254
	Outlet	SST PANS ILES	zeroGradient	-
	Walls	SST PANS	omegaWallFunction	-
		ILES	zeroGradient	-
ε				$\mathrm{m}^2/\mathrm{s}^3$
	Inlet	RNG	fixedValue	15.62
	Outlet	RNG	zeroGradient	-
	Walls	RNG	epsilonWallfunction	-

turbulence dissipation rate was then calculated as:

$$\varepsilon = C_\mu \frac{k^2}{\beta \nu} \tag{3.3}$$

$$\omega = \frac{\varepsilon}{\beta^* k}. \tag{3.4}$$

The PANS model unresolved-to-total turbulence kinetic energy was set to a uniform value of $f_k = 0.4$ leading to $f_\omega = 1/f_k = 2.5$.

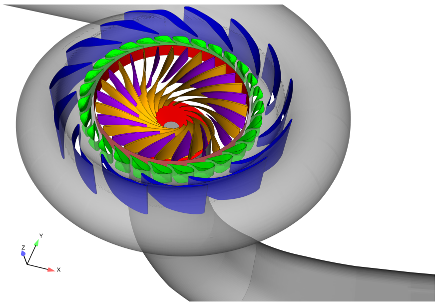

Figure 3.7: *A detailed view of the distributor and runner. The patches in red are the GGI interfaces; the topmost, cylindrical patch is the interface between the guide vane region and the runner, while the patch below the runner blades is the interface between the runner and the draft tube.*

3.2.4 Mesh motion

For the steady operation case mesh rotation was handled by the class *turboFvMesh*, which rotates a chosen region of the mesh by a fixed rotational speed. For the transient load-rejection case a class providing the functionality of flow-driven runner rotation, implemented by Krane [19] was used. This was the only major difference in the simulation setup between the steady and transient operation cases.

3.3 Post-processing

Post-processing of simulation data was done using FOAM-extend utilities, EnSight and Matlab. The utility *sample* in FOAM-extend was used to extract velocity data for comparison with experiments. A probing utility was used to extract raw pressure data, which was processed in Matlab. All pictures was created in the post-processing software EnSight.

3.3.1 Velocity profiles

The averaged velocity field was converted to cylindrical coordinates and sampled at the two lines where experiments were available, described in table 3.4. The axial and tangential velocities were compared to experiments for all turbulence models.

Table 3.4: Velocity profile line locations

	Top Line		Bottom Line	
	Start	End	Start	End
x [m]	-0.1789	0	-0.1965	0
y [m]	0	0	0	0
z [m]	-0.2434	-0.2434	-0.5414	-0.5414

3.3.2 Flow structures

As a qualitative method of analysis the flow structures are used to identify coherent structures, such as the swirling vortex rope. Iso-surfaces of the second invariant of the velocity gradient, or

$$Q = \frac{1}{2}\left(|\Omega|^2 - |S|^2\right), \tag{3.5}$$

was used for visualising the flow structures. A positive Q-criterion represent the regions where Euclidean norm of the vorticity tensor, Ω, is greater than that of the rate of strain, S, i.e. a vortex by the definition of Hunt, Wray, and Moin [16].

3.3.3 Pressure probes

Experimental values of pressure was provided at the locations described in table 3.5 and figure 3.8. In all simulations the outlet pressure was set to 0 kPa, while the outlet pressure in the BEP experiment was 101.562 kPa, and the pressure in the results were adjusted accordingly.

Sensor	x [m]	y [m]	z [m]
VL01	0.2623	0.1935	-0.0296
P42	7.16×10^{-5}	0.1794	-0.0529
S51	-0.08	0.0838	0.0509
P71	-0.0666	0.0423	0.0860
DT11	-0.0904	0.1566	-0.3058
DT12	-0.0904	-0.1566	-0.3058

Table 3.5: Pressure probe locations

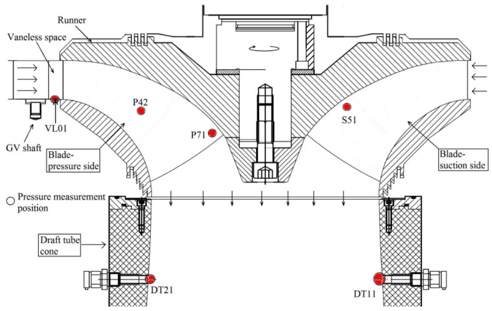

Figure 3.8: *Pressure probe location scheme*

3.3.4 Integral quantities

The integral quantities analysed are head, runner shaft torque and efficiency. The head was evaluated from a difference of total pressure between the spiral casing inlet and the draft tube outlet using equations 2.1 and 2.2. The torque was calculated by integration of the pressure and shear stress over the runner hub, shroud and blades using equation 2.51. The equations used for calculating the integral quantities of the experiments does not account for the head added by the gravitational force. To make a comparison as fair as possible the results are presented both with and without the gravitational term accounted for.

4 Results and Discussion

Transient simulations were carried out using several turbulence models at the best efficiency point operating conditions. Comparisons with experimental data are presented in this chapter. These comparisons include velocity profiles in the draft tube, pressure levels at the probe locations and integral quantities of the flow region. The initial transient of a load-rejection condition were also studied, with main focus on pressure fluctuation levels and runner motion.

4.1 Steady operation

4.1.1 Velocity field

In the majority of the papers presented at the Francis-99 workshop there are major difficulties in predicting tangential velocity at both experimental locations. The use of unsteady simulations that resolve some turbulent scales [36, 17] show a slight increase in accuracy when it comes to tangential velocity profiles. The turbulence modelling has been one of the main subjects in this thesis and some interesting results have been found. The ILES and k-ω SST models are similar in performance with the ILES predicting the tangential velocity better and the SST model predicts the axial velocity better. The SST PANS model did not increase the accuracy of the original SST model, but rather decreased it which was unexpected. This is in no way a definitive result and there can be a number of reasons for this, such as simulation uncertainties or insufficient averaging time.

The steady operation results behave in different ways depending on the turbulence model formulation. There are the pure URANS models: k-ε RNG, k-ω SST, which model all turbulent scales and there are the models that resolve some turbulent scales: k-ω SST-PANS, ILES. There are a substantial difference in the instantaneous flow field between these two approaches as can be seen in figure 4.1. The instantaneous velocity field of the PANS and ILES models reveal some velocity structures that cannot be seen in the SST and RNG models.

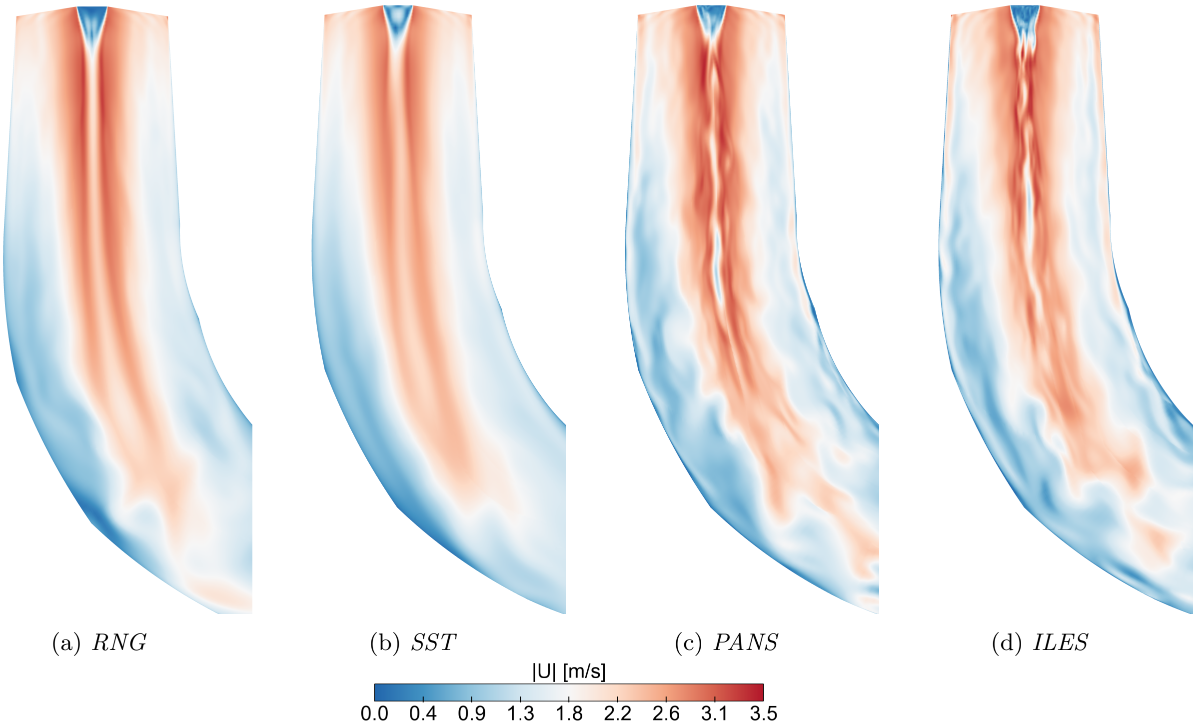

Figure 4.1: *Instantaneous velocity magnitude in the draft tube at a plane y=0.*

When viewing the averaged velocity fields in figure 4.2, it is apparent that there are more similarities. The

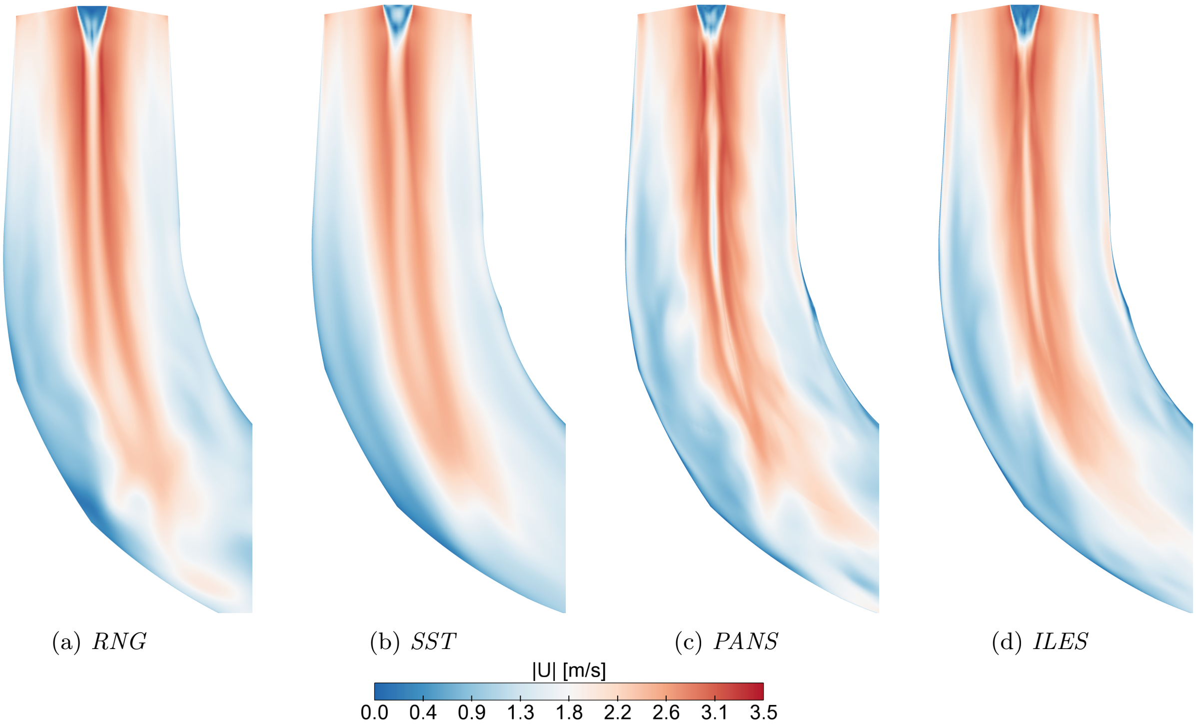

Figure 4.2: *Time averaged velocity magnitude in the draft tube at a plane y=0.*

largest differences when comparing the URANS and resolving models can be seen in the width of the low velocity centre region which is larger for the URANS models. The velocity gradients are also smoother for these models, particularly in the lower part of the draft tube. When looking at the shape of the hub wake some differences between the PANS and ILES models are also visible, whereas for the PANS model the wake looks more like that of the SST model. The PANS model stands out from the rest also in that the velocity magnitude close to the centre is higher than the other models, this can also be seen in the velocity profiles in figure 4.4, especially for the tangential velocity. Some unsteadiness of the PANS and ILES methods is apparent also in the averaged fields, meaning the duration of averaging is insufficient.

A comparison to the experimental velocities at two locations in the draft tube visualised in figure 4.3 is made. In figure 4.4 the velocity profiles are shown, all velocities defined by the original coordinates of the geometry. All of the turbulence models are quite close to the experimental values with the SST and ILES models closest and the PANS model deviating the most. The RNG model is somewhere in between the SST and PANS profiles at most locations. The center of the top line is the location deviating from the experiments the most, especially the RNG model. This is because in the simulations the center of the top line is inside the wake of the runner hub, while in experiments the wake is smaller. At the wall of the bottom line the ILES and PANS models over-predict the axial velocity which indicates that the impact of a turbulence model is not large enough. This assumption is also supported by the fact that the ILES model, which has no turbulence model affecting the flow, over-predicts the velocity more than the PANS model for which 40% of the turbulence is modelled.

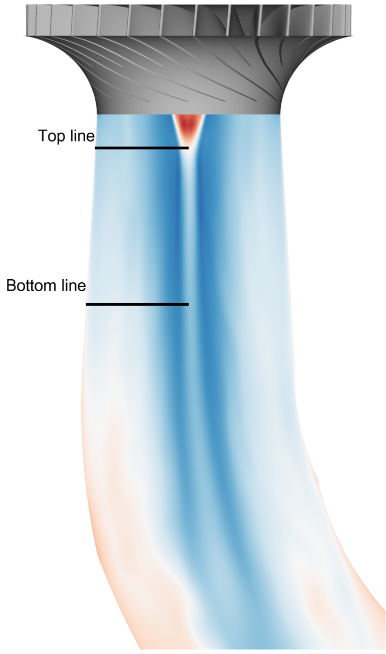

Figure 4.3: *Axial velocity at the plane y=0 in the draft tube and lines where velocity is compared to experiments. Top line:* $z = -0.2434\,\mathrm{m}$*, Bottom line:* $z = -0.5414\,\mathrm{m}$

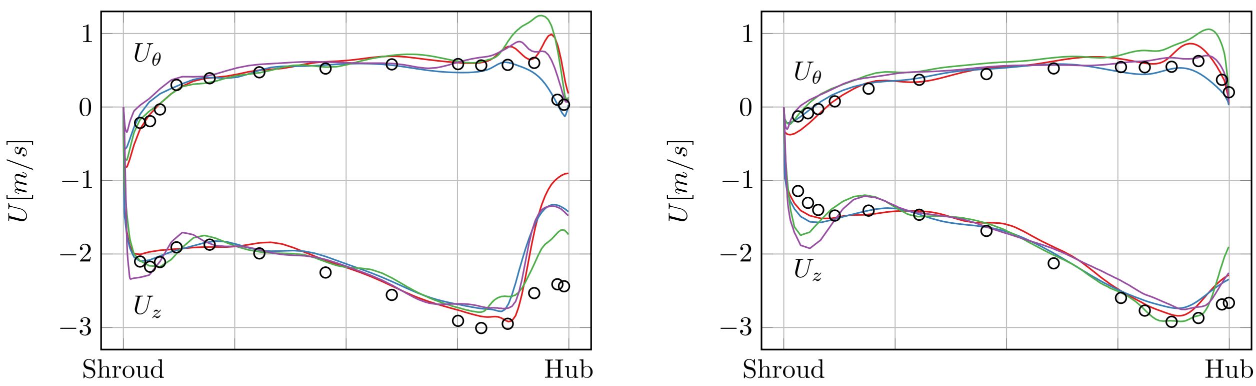

(a) *Axial and tangential velocity at top line*

(b) *Axial and tangential velocity at bottom line*

Figure 4.4: *Time averaged velocity profiles of tangential velocity,* U_θ*, and axial velocity,* U_z*, at two locations in the draft tube compared to experimental values.* — *RNG* — *SST* — *PANS* — *ILES* ○ *Exp*

4.1.2 Flow structures

The flow structure analysis is a qualitative analysis that is based on the expected characteristics of a turbulent flow field. It is likely to have lots of irregular, coherent structures which are unsteady in nature. The smaller and more detailed structures, the higher the resolution of the simulation. It does not, however, always mean that the accuracy is increased. In figure 4.5 a significant difference between the URANS and the resolving models can be seen. Both the RNG and SST models shows the strong, persistent vortex structure in the center region, but they do not capture the weaker, unsteady turbulent structures. The scale-resolving models does capture both the vortex rope and some smaller structures, which is expected. A slight difference can also be seen between the scale-resolving models as the structures of the PANS model, which models 40 % of the turbulent fluctuations, are larger and fewer than those of the ILES model, in which no scales are explicitly modelled. The difference is, however, not very pronounced as the grid resolution is inadequate for ILES simulations.

(a) *RNG* (b) *SST* (c) *PANS* (d) *ILES*

Figure 4.5: *Isosurfaces of Q-criterion = 200 in the draft tube, coloured with pressure.*

The structures at the runner inlet seen in figure figure 4.6 share much more similarities. The RNG, SST and PANS models all show a similarly sized separation at the suction side leading edge of the splitter blade. The main blade does not show the same level of separation, especially for the SST and PANS models. The PANS model also show a little more structures downstream. When looking at the structures of the ILES model the trend is the same as in the draft tube, that more and smaller structures are visible. The leading edge separation seen for the other models is however not apparent here. Some structures can also be seen right at the inlet at the GGI interface, which might be a behaviour caused by the interface itself or because of the resolving of finer scales.

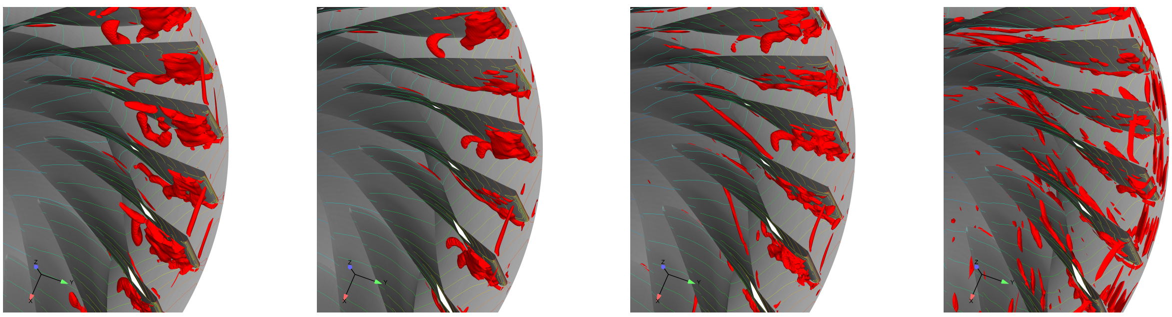

(a) *RNG* (b) *SST* (c) *PANS* (d) *ILES*

Figure 4.6: *Isosurfaces of Q-criterion = 25000 at runner inlet.*

4.1.3 Turbulent quantities

The eddy viscosity is the way of transferring the effect of modelled turbulent fluctuations to the momentum equations. By looking at the eddy viscosity ratio, ν_t/ν, in figure 4.7, the amount of turbulent damping can be observed. A large difference can be seen when comparing the RANS and PANS modelling methods. This is in line with the expected results as more turbulent scales are resolved by the PANS method. One thing to note is that the eddy viscosity of the SST model is higher than that of the RNG model in most locations, which was unexpected because of the limiter in the SST eddy viscosity formulation. The re-normalisation treatment in the RNG ϵ-equation destruction term seems to reduce the eddy viscosity more than the SST limiter. By looking at

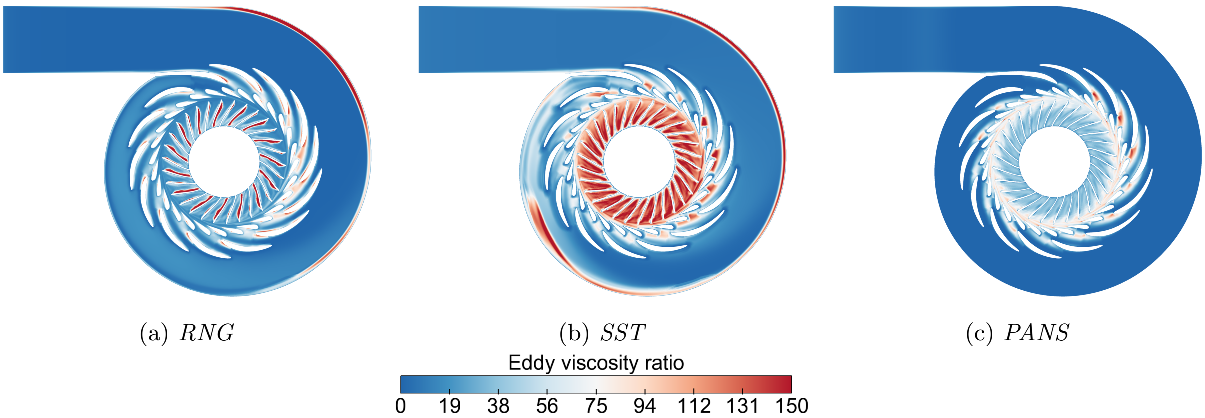

Figure 4.7: *Eddy viscosity ratio in the distributor and runner at a plane $z = 0$.*

the modelled and total turbulence kinetic energy in figure 4.8 the RANS and PANS methods can be compared. The RANS simulation is almost completely steady and the difference between figures 4.8a and 4.8b is very small. In contrast, the resolved energy for the PANS method dominate and most of the scales are resolved.

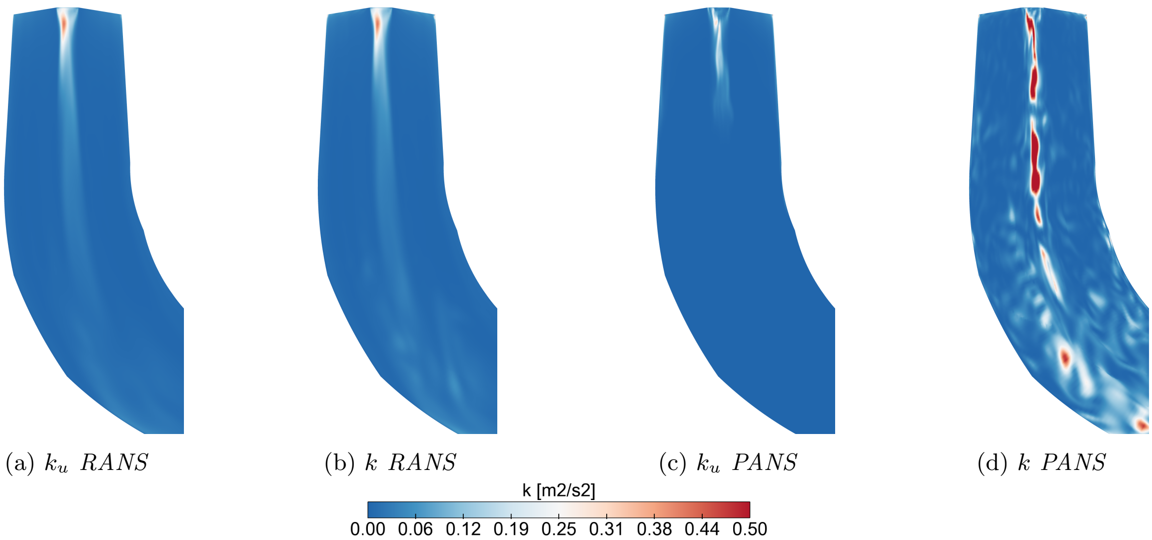

Figure 4.8: *Modelled, k_u, and total turbulence kinetic energy, $k = \frac{1}{2}\overline{u_i'u_i'} + k_u$ in the draft tube at the plane $y = 0$.*

4.1.4 Pressure data

The mean pressure levels of all models are in close correlation with experiments at most locations, although the pressure at the blade suction side probe, S51, is overestimated while the pressure in the draft tube is slightly underestimated. This is in line with previous works. The pressure at VL01 is also overestimated, especially by the RANS models, leading to the difference in head seen in table 4.1.

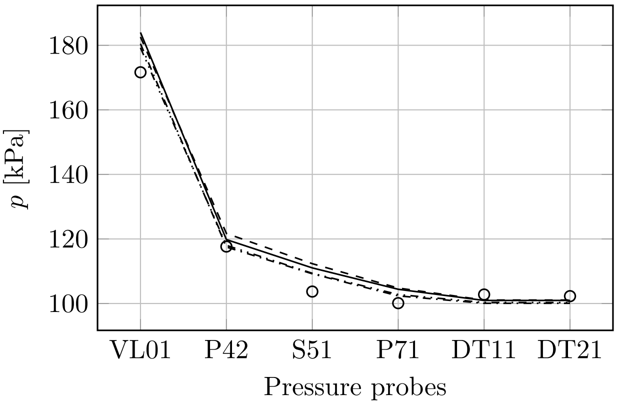

Figure 4.9: *Mean pressure at the pressure probes:*
—— *RNG* - - - *SST* -··- *PANS* -·-·- *ILES*
○ *Exp*

To find the main frequencies of the turbine FFT analysis have been performed on the data from the pressure probes. The frequencies are then compared to the main frequencies of the experiments. As the analysis of the CFD pressure data covers only one revolution low frequencies will not be captured. When comparing the data from the pressure probe VL01 there are good agreement with the main blade passing frequency of $30f_n$. Half the blade passing frequency of about $15f_n$, corresponding to either the main blades or the splitter blades is also captured. When looking at the runner blade probes it can be seen that the main frequency is close to $28f_n$, equal to the number of guide vanes.

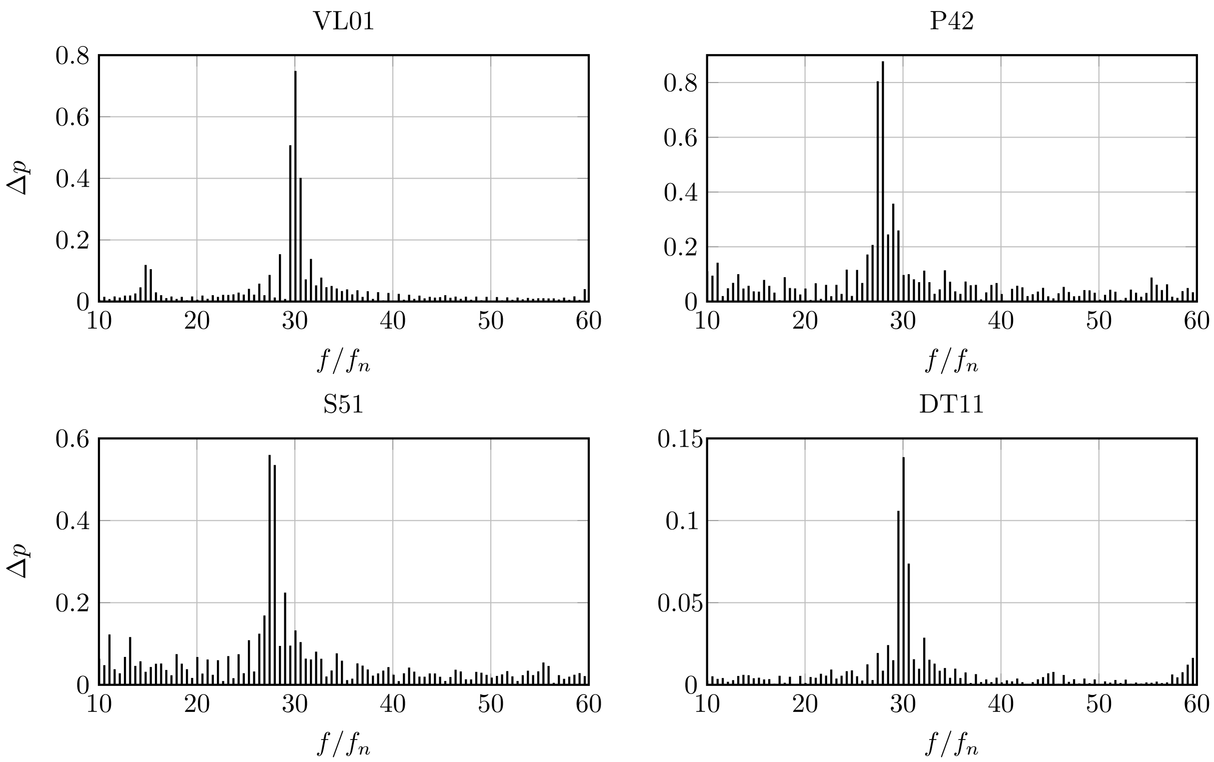

Figure 4.10: *FFT analysis of pressure data for pressure probes VL01, P42, S51 and DT11.*

4.1.5 Integral quantities

The integral quantities represent the total transfer of energy in the system. The head is overestimated by all turbulence models, most by the RNG model (15 %) and least by the ILES (4.8 %). The energy extracted in the form of torque (generator and losses) is overestimated by even more ($12 - 20\%$), with the same models as for the head predicting the highest and lowest values. This discrepancy in estimation of head and torque results in an predicted efficiency deviation of about $3.2 - 5.7\%$ with the k-ω SST model being closest to experiments. As the gravitational term was not included in the total pressure definition of the workshop it has not been included here. If gravitational effects had been included in the simulations the total head would have been about 5 % higher. The results with and without the gravitational term added are shown in table 4.1.

Table 4.1: Integral quantities by Francis-99 (equation 2.2) and IEC (equation 2.3) total pressure definitions

		F-99			IEC		
Turbulence Model	T [N m]	Δp_0 [kPa]	H [m]	η [%]	Δp_0 [kPa]	H [m]	η [%]
Experiment	619.6	117.5	11.91	92.61	-	-	-
$k - \varepsilon$ RNG	742.8	133.9	13.67	95.81	140.5	14.32	91.48
$k - \omega$ SST	718.8	129.0	13.26	95.57	136.5	13.91	91.13
$k - \omega$ SST PANS	705.8	127.6	13.00	95.74	133.9	13.65	91.20
ILES	693.3	122.5	12.48	97.90	128.9	13.13	93.08

4.2 Transient operation

The load-rejection case shows some interesting results. One thing to note in figure 4.11a is that the rotational speed increase is linear, which can be explained by a linearly decreasing but oscillating flow torque in figure 4.12a leading to the high angular acceleration seen in figure 4.11b. Just at the moment of load loss, however, the hydraulic torque suddenly drops from 712 Nm to 470 Nm, as seen in figure 4.12b. Whether this is a physical phenomenon or a consequence of numerics is hard to judge. Furthermore, no discontinuity of the rotational speed in respect to time can be seen. It is not very strange that these high gradients occur as there is a very sudden change of the limiting torque in just one time step. There is a possibility that the reaction could be smoother with a smaller time step, but there is also the possibility that the transient is close to discontinuous, and no further accuracy is gained by reducing the time step.

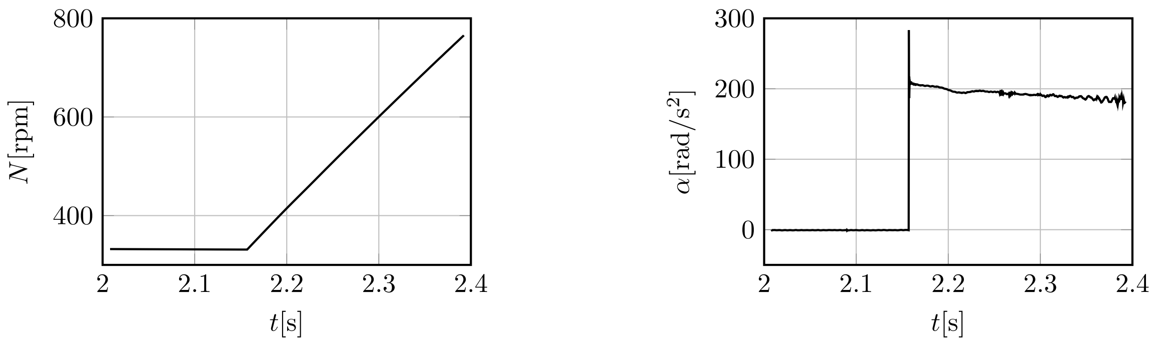

(a) *Rotational speed*

(b) *Angular acceleration*

Figure 4.11: *The motion state of the runner, showing rotational speed and acceleration before and after the torque loss.*

The other question concerns the high angular acceleration observed. In experiments Trivedi [37] found that the acceleration of the runner during a load-rejection event from about 25% rotational speed to the runaway speed of 136% for the BEP takes 1.7 s. This equates to an angular acceleration of about 23 rad/s^2. In the current simulation the rotational speed has increased to over 200% of the constant rotational speed in 0.25 s, and the angular acceleration, seen in figure 4.11b is roughly ten times that of Trivedi. There are some major differences between the two, which greatly affects the results. In the experiments the guide vanes are closed during the event and the inlet flow rate decreases during the runner acceleration, as opposed to the simulation where the constant flow rate results in an increasing total pressure difference. Another uncertainty is the moment of inertia, which has been estimated to $2.5\,\mathrm{kg\,m^2}$. This is only an approximation, but it is unlikely that this will differ by one order of magnitude. Hence, the probable cause for the high acceleration is a combination of the two.

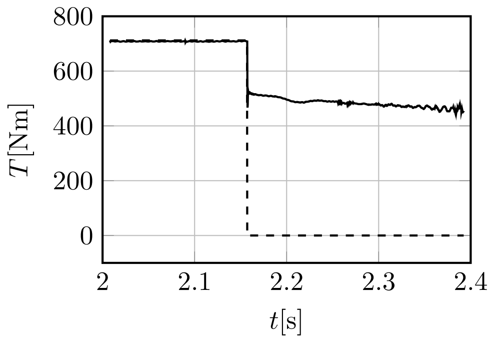

(a) $t < 2.15\,\mathrm{s}$: *Oscillating flow torque with a small amplitude.* $2.15\,\mathrm{s} < t$: *Decreasing flow torque after sudden load loss.*

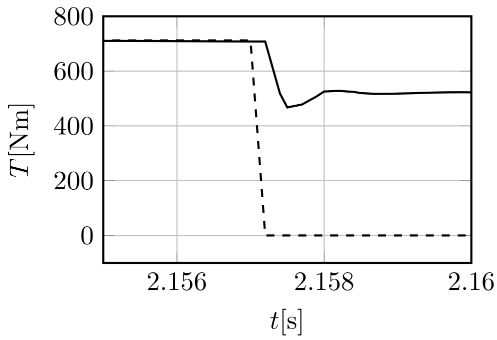

(b) *An enlargement of the moment of sudden shaft torque loss.*

Figure 4.12: *Torques affecting the runner rotation,* —— *Hydraulic torque* - - - *Shaft torque.*

4.2.1 Comparison of instantaneous work

Total pressure and tangential velocity at the runner inlet and outlet have been extracted at two time steps. At t=1.62368 when the runner is rotating with a constant frequency and at t=2.38231 when the runner is accelerating. It should be noted that all variables are instantaneous and should not be compared to the averaged values presented in table 4.1. By using equation 2.7, converted to rpm

$$N_{max} = \frac{30}{\pi} \frac{\Delta p_0}{\rho \left(r_2 c_{\theta 2} - r_3 c_{\theta 3} \right)}, \tag{4.1}$$

an approxiamtion of the maximum rotational speed can be made. The tangential velocity and total pressure are taken from the simulation results and averaged over the runner inlet and outlet. Equation 4.1 results in a potential maximum rotational speed of $N_{max} = 537.8\,\mathrm{rpm}$ for the steady case which is close to the runaway speed obtained by Trivedi [37] of $N_{max} = 524.4\,\mathrm{rpm}$. For the accelerating case $N_{max} = 1331\,\mathrm{rpm}$, which is in a reasonable range as the runner is still accelerating. In table 4.2 the motion state of the two instances in time can be seen.

Table 4.2: Results for the transient operation simulations for two time steps. During steady operation, t=1.62368; and during transient operation, t=2.38231.

State	*Time*	N[rpm]	α[rad/s^2]	I_Z	T_{shaft}	T_h	Δp_0[kPa]	Δc_θ	N_{max}[rpm]
Steady	1.62368	-335.4	0.4	5	712	-710	118.7	6.653	-537.8
Accelerating	2.38231	-756.7	-185.3	2.5	0	-463.3	279.1	5.725	-1331

4.2.2 Pressure data

The pressure data of the load-rejection case is presented in figure 4.13. At VL01 the pressure drops instantly by 12 kPa and is then constantly increasing until the simulation is stopped. In DT11 there is a short instability with an amplitude of 10 kPa before the pressure start rising. The pressure increase is much lower than that of VL01, resulting in an overall pressure difference increase, which is in agreement with previous results. The reason for the increasing amplitude of the fluctuations at both pressure probes can possibly be caused by flow transients. A more likely explanation, however, is that the increased pressure difference before and after the runner increases the amplitudes of the fluctuations.

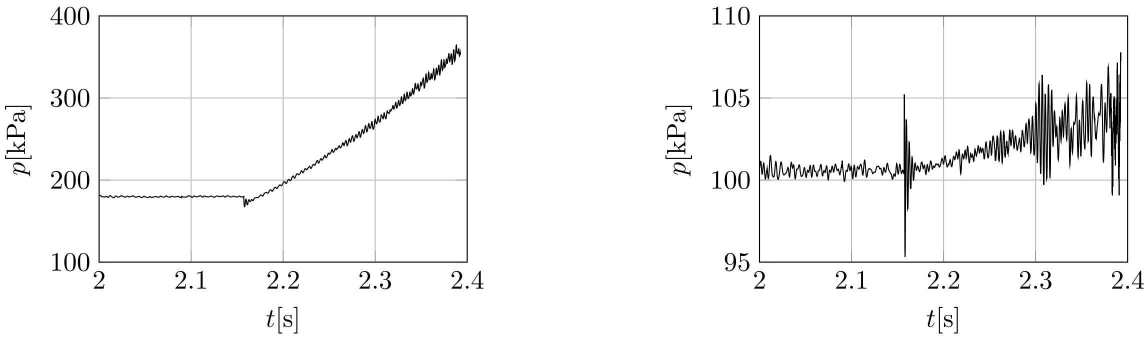

(a) *VL01* (b) *DT11*

Figure 4.13: *The evolution of pressure for two pressure probes during the initial transient of the load-rejection simulation.*

5 Conclusions

In the present work the flow in the Francis-99 high head model turbine have been investigated. Simulations at steady and transient operation have been performed. In the steady operation case the best efficiency point operating condition was simulated and several turbulence models were evaluated and compared to experiments. For the unsteady operation case the initial transient of a sudden load-rejection event is simulated and analysed.

The agreement with experiments of draft tube velocity profiles was good for all turbulence models. This is an indication of the turbulence modelling being of minor importance in this particular measurement. As the high swirl velocity in the center of the draft tube was decreased by the ILES model it is evident that under-resolved implicit LES simulations can predict the flow field accurately, despite the use of unsuitable schemes and coarse meshes. This indicates a limited influence of small scale turbulence on the flow or possibly adequate numeric dissipation by the current numerical schemes. As the mean velocity field is clearly not fully averaged for the PANS and ILES models after one revolution it is likely that scale-resolving methods need a longer averaging time than URANS methods. Despite the performance of the current PANS method being worse than the original RANS k-ω SST model in most aspects the hopes for PANS is still high. There are many uncertainties regarding the current implementation and further investigation is needed before drawing any conclusions.

The overestimated efficiency of the Francis-99 turbine at BEP is mainly due to the definition of total pressure by the workshop organisers, as the prediction becomes very good when accounting for the lack of gravity forces in the CFD simulations. As the efficiency prediction proved very good when accounting for gravity, it is likely the seal friction does not have a large impact on efficiency at the best efficiency operating condition. The main pressure frequencies are captured, but should any lower frequency, such as that of a vortex rope be of interest, the averaging time of only one revolution would not suffice.

The implemented flow-driven mesh motion functionality rotates the mesh in a robust and predictable way, and it is a good functionality to have for operation at an unknown rotational speed. FOAM-extend is judged to be a good framework for the implementation and modification of tools enabling and simplifying the simulations of turbines at transient operation. When performing such simulations it becomes increasingly important to use the right boundary conditions if realistic results are the objective. It was found that realistic boundary conditions are a prerequisite for realistic results. Another requirement for realistic simulations during transient operation is the knowledge of turbine data, such as moment of inertia and friction torques.

Finally, it is the hope and belief of the author that this work have contributed to an increased insight in the branch of variable resolution turbulence modelling, for the application of hydroelectric turbines and in general. Furthermore, it has been shown that flow-driven runner rotation can be applied to an industry-size case using FOAM-extend, taking a step towards high-fidelity numeric simulations of high-head Francis turbines in unsteady operation.

6 Future Work

6.1 Mesh study

The mesh provided by the workshop and modified by Lucien Stoessel was further improved, however, the quality is still not adequate. A thorough mesh study including different meshing methods; such as structured or unstructured topology, hexahedra, tetrahedra or other polyhedra, automatically or manually generated, grid resolution, wall spacing, and so on. In many areas of CFD the quality of the mesh is the single most important parameter for a successful simulation.

6.2 Turbulence modelling

As pointed out in the previous chapter the turbulence modelling did not have a large impact on the averaged flow field. The prediction of efficiency and the instantaneous flow field does however depend a lot on the selection of model. Particularly the investigation of RANS-LES models such as PANS and DDES should be of great interest when transient simulations can be considered. A dynamic PANS model could prove a valid candidate for such an investigation as it efficiently tries to utilise the potential of the mesh in terms of resolving velocity fluctuations, see appendix A. It does however need validation on known benchmark cases. Higher level under-resolved methods such as ILES and VLES should be evaluated using proper numerical treatment.

6.3 The mechanical system

To accurately predict the efficiency of a turbine it is not enough to solve the flow accurately. The systems that interact with the turbine also have to be taken into account. Particularly the leakage flow and seal friction are important to the efficiency prediction. Therefore, it would be of great interest to investigate the modelling of such systems and couple them to the running CFD simulation. On a similar topic is the dynamic system of the turbine-generator interaction. For realistic simulations of transient operation including flow-driven runner motion the moments of inertia of the runner and generator have to be utilised. Also the dynamics of the generator itself and the electric grid might be included in future investigations.

6.4 Transient operation

There are several more transient operation scenarios that is of interest. The next step should be the runaway case, which is a fairly simple one. Also load-acceptance and load-rejection with moving guide vanes should be possible. For many of these transient simulations the development of new mesh motion implementations would have great effect on the ability to simulate these transient scenarios. For this specialised use FOAM-extend is a very good contender, although there are other software packages offering similar functionality. A prerequisite for performing realistic simulations of transient operation is the usage of correct boundary conditions, for which the rotational speed and inlet total pressure are coupled, for example.

References

[1] B. Aakti et al. “On the performance of a high head Francis turbine at design and off-design conditions”. *Francis-99 Workshop*. Trondheim, 2014.

[2] B. Basara, S. Krajnović, and S. Girimaji. “PANS vs. LES for computations of the flow around a 3D bluff body”. *7th International ERCOFTAC Symposium on “Engineering Turbulence Modelling and Measurements”*. Limassol, Cyprus, 2008.

[3] M. Beaudoin and H. Jasak. “Development of a Generalized Grid Interface for Turbomachinery simulations with OpenFOAM”. *Open Source CFD International Conference*. Berlin, Germany, 2008.

[4] J. P. Boris. On large eddy simulation using subgrid turbulence models. *Whither Turbulence? Turbulence at the Crossroads* J.L. Lumley (Ed) (1990), 344–353.

[5] D. Celic and H. Ondracka. “The influence of disc friction losses and labyrinth losses on efficiency of high head Francis turbine”. *Francis-99 Workshop*. Trondheim, 2014.

[6] G. Chen et al. “OpenFOAM computation of interacting wind turbine flows and control (I): free rotating case”. 2014.

[7] L. Davidson. The PANS k-epsilon model in a zonal hybrid RANS-LES formulation. *International Journal of Heat and Fluid Flow* **46** (2014), 112–126.

[8] S. L. Dixon and C. A. Hall. *Fluid Mechanics and Thermodynamics of Turbomachinery*. 7th Editio. 2013.

[9] H. Foroutan and S. Yavuzkurt. A partially-averaged Navier–Stokes model for the simulation of turbulent swirling flow with vortex breakdown. *International Journal of Heat and Fluid Flow* **50** (2014), 402–416.

[10] S. Girimaji. Partially-Averaged Navier-Stokes Model for Turbulence: A Reynolds-Averaged Navier-Stokes to Direct Numerical Simulation Bridging Method. *Journal of Applied Mechanics* **73**.3 (2006), 413–421.

[11] S. Girimaji and K. Abdol-Hamid. “Partially-Averaged Navier Stokes Model for Turbulence: Implementation and Validation”. *43rd AIAA Aerospace Sciences Meeting and Exhibit*. Reno, USA, 2005.

[12] S. Girimaji and S. Wallin. Closure modeling in bridging regions of variable-resolution (VR) turbulence computations. *Journal of Turbulence* **14**.1 (2013), 72–98.

[13] F. F. Grinstein and C. Fureby. On Flux-Limiting-Based Implicit Large Eddy Simulation. *Journal of Fluids Engineering* **129**.12 (2007), 1483.

[14] W. Gyllenram. Very Large Eddy Simulation of Draft Tube Flow Turbulence modeling. *23rd IAHR Symposium* (2006).

[15] K. Hanjalić, M. Popovac, and M. Hadžiabdić. A robust near-wall elliptic-relaxation eddy-viscosity turbulence model for CFD. *International Journal of Heat and Fluid Flow* **25**.6 (2004), 1047–1051.

[16] J. C. R. Hunt, A. A. Wray, and P. Moin. *Eddies, streams, and convergence zones in turbulent flows*. 1988.

[17] D. Jost et al. “Numerical simulation of flow in a high head Francis turbine with prediction of efficiency, rotor stator interaction and vortex structures in the draft tube”. *Francis-99 Workshop*. Trondheim, 2014.

[18] S. Krajnović, R. Lárusson, and B. Basara. Superiority of PANS compared to LES in predicting a rudimentary landing gear flow with affordable meshes. *International Journal of Heat and Fluid Flow* **37** (2012), 109–122.

[19] E. Krane. *A tutorial on modification of the turboFvMesh class for flow-driven rotation*. Tech. rep. 2014.

[20] S. Lakshmipathy and V. Togiti. “Assessment of Alternative Formulations for the Specific-Dissipation Rate in RANS and Variable-Resolution Turbulence Models”. *20th AIAA Computational Fluid Dynamics Conference*. June. Honululu, USA, 2011, pp. 1–20.

[21] B. van Leer. Towards the Ultimate Conservative Difference Scheme. V. A Second-Order Sequel to Godunov's Method. *Journal of Computational Physics* **32**.1 (1979), 101–136.

[22] L. G. Margolin, W. J. Rider, and F. F. Grinstein. Modeling turbulent flow with implicit LES. *Journal of Turbulence* **7**.May 2015 (2006).

[23] F. R. Menter. Two-Equation Eddy-Viscosity Turbulence Models for Engineering Applications. *AIAA Journal* **32**.8 (1994).

[24] A. V. Minakov et al. “Numerical modeling of flow in the Francis-99 turbine with Reynolds stress model and detached eddy simulation method”. *Francis-99 Workshop*. Trondheim, 2014.

[25] P. Mössinger, Jester-Zürker, and A. Jung. “Investigation of different simulation approaches on a high-head Francis turbine and comparison with model test data: Francis-99”. *Francis-99 Workshop*. Trondheim, 2014.

[26] J. Nicolle and S. Cupillard. “Prediction of dynamic blade loading of the Francis-99 turbine”. *Francis-99 Workshop*. Trondheim, 2014.

[27] H. Nilsson. Evaluation of OpenFOAM for CFD of Turbulent Flow in Water Turbines. *23rd IAHR Symposium* (2006), 1–9.

[28] M. Page, M. Beaudoin, and A.-M. Giroux. Steady-state Capabilities for Hydroturbines with OpenFOAM. *International Journal of Fluid Machinery and Systems* **4**.1 (Mar. 2011), 161–171.

[29] O. Petit. "Towards Full Predictions of the Unsteady Incompressible Flow in Rotating Machines , Using OpenFOAM". PhD thesis. 2012.

[30] P. K. Smolarkiewicz. A Simple Positive Definite Advection Scheme with Small Implicit Diffusion. *Monthly Weather Review* **111**.3 (1983), 479–486.

[31] P. K. Smolarkiewicz. MPDATA: A Finite-Difference Solver for Geophysical Flows, *Journal of Computational Physics* **140** (1998), 459–480.

[32] P. R. Spalart and M. Shur. On the sensitization of turbulence models to rotation and curvature. *Aerospace Science and Technology* **1**.5 (1997), 297–302.

[33] C. G. Speziale. "Computing non-equilibrium turbulent flows with time-dependent RANS and VLES". *15th international conference on numerical methods in fluid dynamics*. Monterey, USA, 1996.

[34] C. G. Speziale, S. Sarkar, and T. B. Gatski. Modeling the Pressure-Strain Correlation of Turbulence - An Invariant Dynamical Systems Approach. *Journal of Fluid Mechanics* **227**.June 1991 (1991), 245–272.

[35] L. Stoessel. "Numerical simulations of the flow in the Francis-99 turbine". PhD thesis. 2014.

[36] L. Stoessel. "Steady and unsteady numerical simulations of the flow in the Tokke Francis turbine model, at three operating conditions". *Francis-99 Workshop*. Trondheim, 2014.

[37] C. Trivedi. "Investigations of Transient Pressure Loading on a High Head Francis Turbine". PhD thesis. LuleåUniversity of Technology, 2014.

[38] C. Trivedi et al. Experimental and Numerical Studies for a High Head Francis Turbine at Several Operating Points. *Journal of Fluids Engineering* **135**.11 (Aug. 2013), 111102.

[39] C. Trivedi et al. Transient Pressure Measurements on a High Head Model Francis Turbine During Emergency Shutdown, Total Load Rejection, and Runaway. *Journal of Fluids Engineering* **Jun**.12 (Sept. 2014), Accepted for publication.

[40] S. Wallin. "Engineering turbulence modelling for CFD with a focus on explicit algebraic reynolds stress models". PhD thesis. Kungliga Tekniska Högskolan, 2000.

[41] V. Yakhot et al. Development of turbulence models for shear flows by a double expansion technique. *Physics of Fluids* **4**.May 2015 (1992).

[42] M. Zreik. "A computational study of the unsteady flow past tandem cylinders". PhD thesis. The University of Alabama, 2006.

Appendices

A The k-ω SST PANS turbulence model

Simulations using the dynamic PANS model was initiated but unfortunately never finalised due to the time demanding evolution of f_k throughout the domain. The model was however tested on the OpenFOAM tutorial case axialTurbine to verify the functionality. The k-ω SST PANS model was implemented with two formulations of unresolved-to-total turbulent kinetic energy, f_k. The one presented in the thesis used a fixed value of $f_k = 0.4$. A dynamic formulation,

$$f_k = 1 - \left[\frac{\left(\frac{\Lambda}{\Delta}\right)^{2/3}}{0.23 + \left(\frac{\Lambda}{\Delta}\right)^{2/3}} \right]^{9/2}, \tag{2.41}$$

developed in [9] was also implemented with the objective to resolve as much of the turbulent scales the mesh resolution would allow. There are two ways to implement the formulation, one way is to base the f_k-value on a previous RANS simulation and keep it fixed in time. The other option, which was chosen for this test case, is to change the f_k-value for every point in space and time.

A.1 The axialTurbine case

To test new implementations the FOAM-extend tutorial case *axialTurbine* have been used throughout the project. The geometry is visualised in figure A.1, although only one blade passage is simulated. The inlet velocity is 1 m/s and the outlet pressure is zero, the rotational speed is constant at 10 rad/s. The k-ω SST PANS model with dynamic f_k is tested, and in figure A.2 the evolution of f_k in time can be seen. The initial condition of f_k is 0.4 in the whole region, the values at the walls are fixed to unity and zeroGradient conditions are applied at inlet and outlet. It can be seen in figure A.2 that a pulse of f_k travels through the domain to finally be "flushed out". At $t = 1.75$ s f_k is stabilised and the high values are located where the ratio of turbulent-to-grid length scale is low and the other way around.

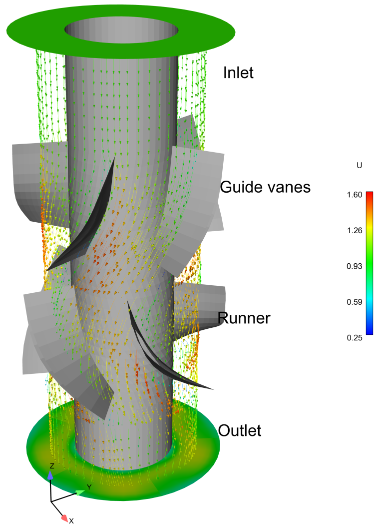

Figure A.1: *The axialTurbine case geometry and velocity vectors.*

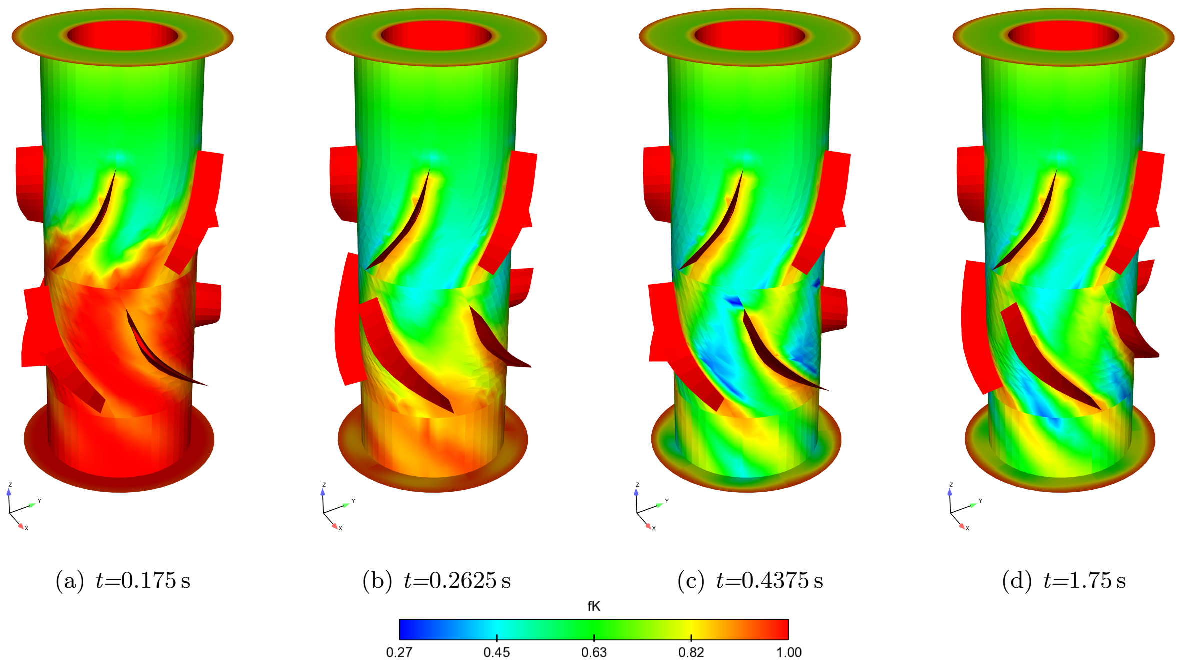

Figure A.2: *The evolution of unresolved-to-total kinetic energy, f_k for the dynamic PANS model.*

B Turbulence modelling coefficients

Table B.1: Turbulence model coefficients

Coefficient	Value
C_μ	0.0845
C_1	1.42
C_2	1.68
α_k	1.39
α_ε	1.39
η_0	4.38
β	0.012

(a) Coefficients for the k-ε RNG model.

Coefficient	Value
α_{k1}	0.85034
α_{k2}	1.0
$\alpha_{\omega 1}$	0.5
$\alpha_{\omega 2}$	0.85616
γ_1	0.5532
γ_2	0.4403
β_1	0.075
β_2	0.828
β^*	0.09
a_1	0.31
c_1	10
C_μ	0.09

(b) Coefficients for the RANS and PANS k-ω SST models.